NUMERICAL STUDY ON THE EXCITATION-DEPENDENT NONLINEAR BEHAVIOR OF DISTRIBUTED MICROCRACKS

A Thesis
Presented to
The Academic Faculty

By

Marius M. Goletz

In Partial Fulfillment
of the Requirements for the Degree
Master of Science in Engineering Science and Mechanics in the
School of Civil and Environmental Engineering

Georgia Institute of Technology

December 2019

NUMERICAL STUDY ON THE EXCITATION-DEPENDENT NONLINEAR BEHAVIOR OF DISTRIBUTED MICROCRACKS

Approved by:

Prof. Laurence J. Jacobs, Advisor
School of Civil and Environmental Engineering
Georgia Institute of Technology

Dr. Jin-Yeon Kim
School of Civil and Environmental Engineering
Georgia Institute of Technology

Dr. Jianmin Qu
School of Engineering
Tufts University

Date Approved: August 23, 2019

ACKNOWLEDGEMENTS

First of all, I want to thank my advisor Dr. Laurence J. Jacobs for all of his support throughout my graduate studies at Georgia Tech. I am grateful for having him as an outstanding advisor, not only due to his excellent professional competence, but also due to his gorgeous human nature. Without his commitment, neither my studies nor the research would have been possible. In addition, I highly appreciate the opportunity to present my research at the Quantitative Evaluation Conference (QNDE) in Portland, Oregon.

My gratitude goes also to Dr. Jin-Yeon Kim for his invaluable advice and constructive discussions throughout this whole research. Especially his excellent experience in research and broad knowledge in this field of research, made him irreplaceable.

Furthermore, I want to thank Dr. Jianmin Qu for being part of the committee and reviewing this thesis.

I would like to thank my labmates Aurelio Bellotti, Brian Fuchs, and Katie Scott for supporting and giving clues at any time.

Moreover, my gratefulness goes to Dr. Thomas Meurer, Mike Anderson, and the PACE support team for their help and advice regarding computational and numerical issues.

Also, I would like to thank my friends and exchange partners Denis Pfeifer and Daniel Niklas Fahse for their support and the interesting discussions at work, and for creating unforgettable memories throughout our whole stay.

Furthermore, I would like to express my thankfulness to Professor Michael Hanss, Professor Peter Eberhard, Dominik Hose, and Sibylle Langer at the University of Stuttgart for their commitment in coordinating this unique program of studying abroad.

Beyond that, I am very grateful for the generous financial support of THE SCHAU-

FLER FOUNDATION and the DAAD (German Academic Exchange Service) via a PROMOS scholarship.

Finally, I want to thank my family and friends to the fullest for their commitment and support.

TABLE OF CONTENTS

Acknowledgments v

List of Tables x

List of Figures xi

Chapter 1: Introduction 1

1.1 Motivation 1

1.1.1 Nonlinear Ultrasound and Second Harmonic Generation Techniques 1

1.1.2 Micromechanics Models 2

1.1.3 Application - Nanostructured Ferritic Alloys (NFA) 3

1.2 Objective 4

1.3 Outline 6

Chapter 2: Wave Propagation 7

2.1 Linear Wave Propagation 7

2.2 Nonlinear Wave Propagation 9

Chapter 3: Background - Combined Micromechanics Model 12

3.1 Bilinear Stiffness Model 12

3.2 Rough Surface Contact Model 13

3.3 Combined Model 13

3.3.1 Main Idea 13

3.3.2 Numerical Values of Material Properties 14

3.3.3 Acoustic Nonlinearity Parameter β 14

3.3.4 Transitions ε_1 and ε_2 16

3.3.5 Nonlinear Stress-Strain Relationship and Resulting Wave Equation 18

3.3.6 Pertubation Approach 19

Chapter 4: Theory of Hyperbolic Partial Differential Equations . . . 21

4.1 Scalar Hyperbolic Equations 22

4.2 Systems of Hyperbolic Equations 24

4.2.1 System Classification 24

4.2.2 Hyperbolicity and Characteristics 25

4.3 Systems of Conservation Laws 29

4.3.1 Integral and Differential Form 29

4.3.2 Problem Formulations 31

Chapter 5: Finite Difference Schemes for One-Dimensional Systems 33

5.1 General Concepts 34

5.2 Upwind vs. Central Schemes 38

5.3 Kurganov-Levy Scheme 41

Chapter 6: Simulation Setup 44

6.1 Solution Procedure 44
6.2 Conservation Form 45
6.3 Initial Conditions 46
6.4 Signal Processing 48
6.5 Numerical Parameters 50
6.5.1 Propagation Distance x_p 50
6.5.2 Spatial Discretization Δx 50
6.5.3 CFL Condition 53

Chapter 7: Results 56

7.1 Quadratic Nonlinearity - Relation between A_1, A_2, and β_{RSC} 58
7.2 Quadratic Nonlinearity - Dependency on Crack Parameters 61
7.2.1 Number of Cracks per cubic meter N_0 62
7.2.2 Crack Radius R 64
7.3 Full Model - Dependency on Crack Parameters 66
7.3.1 Number of Cracks per cubic meter N_0 71
7.3.2 Crack Radius R 74

Chapter 8: Conclusion and Future Work 76

8.1 Conclusion 76
8.2 Future Work 78

References 82

LIST OF TABLES

3.1 Numerical material parameters for NFAs [18] 14

7.1 Numerical material parameters for NFAs [18] 57

7.2 Parameter combinations of h_S and d_0 with the resulting β_{RSC}-values and transitions ε_1,ε_2 59

7.3 Parameter variation of N_0 and the resulting values for the crack density c, β_{RSC} and transitions ε_1,ε_2 63

7.4 Parameter variation of R and the resulting values for the crack density c, β_{RSC} and transitions ε_1,ε_2 65

7.5 Variation of the parameter N_0 72

7.6 Variation of the parameter R 74

LIST OF FIGURES

1.1 Schematic microstructure of NFAs [20] 5

1.2 Scanning electron microscope image of NFA specimen [20] 5

2.1 Infinitesimal volume element dV of a rod exposed to a stress field $\sigma(x,t)$ 8

2.2 Higher harmonics generation of nonlinear media compared to linear media 10

3.1 Schematic stress-strain relationship based on a bilinear stiffness approach 13

3.2 Schematic of the overall nonlinear stess-strain relationship of the combined model adapted from [18] 17

5.1 Numerical domain of dependence (hatched) for a 3-point scheme (x_j,t_n) 36

5.2 Upwind differencing approach for piecewise constant solution with the dotted lines denoting the local Riemann problems 39

5.3 Central differencing approach for piecewise constant solution with the dotted lines denoting the local Riemann problem 40

6.1 Schematic of the solution procedure of the one-dimensional wave equation with the nonlinear stress-strain relationship of the combined model adapted from [43] 45

6.2 Initial strain input $u_2(x,0)$ 48

6.3 Tailoring of the numerical results for the FFT analysis 49

6.4 Numerical solution for the linear wave equation of the Kurganov-Levy scheme with a spatial discretization of $\Delta x = 10^{-6}$m (red dotted line) and $\Delta x = 10^{-5}$m (blue solid line) 52

6.5 FFT result of the numerical solution for the linear wave equation with a spatial discretization of $\Delta x = 10^{-6}$m (red dotted line) and $\Delta x = 10^{-5}$m (blue solid line) 52

6.6 Numerical results for the linear (a),(b),(e) and nonlinear (c),(d),(f) wave equation with CFL conditions of 0.4 (dotted red line) and 0.01 (solid blue line) 55

7.1 Schematic of the overall nonlinear stess-strain relationship of the combined model adapted from [18] 56

7.2 Ratio of the first and second harmonic $\frac{A_2}{A_1^2}$ over the acoustic nonlinearity parameter β_{RSC} 60

7.3 Dependency of the acoustic nonlinearity parameter β_{RSC} on the crack parameters N_0 and R according to the combined model 62

7.4 Dependency of the simulated strain amplitude ratio $\frac{A_2}{A_1^2}$ (red line with circled data points) assigned to the left y-axis and dependency of the acoustic nonlinearity parameter β_{RSC} (blue line with crossed date points) assigned to the right y-axis on the number of cracks per cubic meter N_0 64

7.5 Dependency of the simulated strain amplitude ratio $\frac{A_2}{A_1^2}$ (red line with circled data points) assigned to the left y-axis and dependency of the acoustic nonlinearity parameter β_{RSC} (blue line with crossed data points) assigned to the right y-axis on the crack radius R 66

7.6 Strain amplitude ratio $\frac{A_2}{A_1^2}$ with corresponding acoustic nonlinearity parameter β_{RSC} 68

7.7 Numerical results for a high-amplitude strain wave after propagation for different β_{RSC} values. For low β_{RSC} (a) the wave form looks undistorted. From (b) to (c) the linear relationship breaks down. (d) already depicts the characteristic sawtooth waveform. And (e) and (f) clearly indicate shock wave formation 69

7.8 Example of the dependency of the transitions ε_1 and ε_2 on the acoustic nonlinearity parameter β_{RSC} for different numbers of cracks (a) $N_0 = 4 \cdot 10^7$ $[m^{-3}]$ and (b) $N_0 = 3 \cdot 10^8 [m^{-3}]$ 70

7.9 Dependency of the simulated strain amplitude ratio $\frac{A_2}{A_1^2}$ on the number of cracks per cubic meter N_0 for below, partially, completely, and far above the transitions, where the full model comes into consideration . 72

7.10 Dependency of the simulated strain amplitude ratio $\frac{A_2}{A_1^2}$ on the crack radius R for below, partially, completely, and far above the transitions, where the full model comes into consideration 74

SUMMARY

Since it is well known that microcracks generate higher harmonics in propagating monochromatic waves, there exist different approaches to model this phenomenon. Recent research from Hoffmann et al. combined a Bilinear Stiffness model and a Rough Surface Contact model for a more complete description of the nonlinear behavior of materials containing distributed microcracks. This model intends to be utilized to simulate second harmonic generation in dependence of characteristic crack parameters, e.g. crack radius and number of cracks. The materials considered in this context are Nanostructured ferritic alloys (NFA).

This research presents a numerical approach to determine this dependency, since other methods like the pertubation method fail due to the strong nonlinear effects occurring in such materials. In the first instance, the problem is formulated as a hyperbolic system of conservation laws, before it is implemented and solved with a semi-discrete central scheme. The numerical results are then studied using the signal-processing tool fast Fourier transform (FFT) in order to analyse and interpret the nonlinear effects. To ensure on the one hand, that numerical algorithm works properly and on the other hand, to understand and interpret the results, the problem is approached step by step. After validating the numerical scheme for a linear problem, only the quadratic part of the combined model is examined for varying crack parameters. In a next step, the full model is investigated for different crack parameters. This procedure allows to better understand the evolution and physical interpretation of the strong nonlinear effect observed when the full model is considered.

CHAPTER 1
INTRODUCTION

1.1 Motivation

Nondestructive evaluation (NDE) is a commonly used approach to characterize material damage in various applications. These applications range from energy, and transportation to construction industries, where high safety standards have to be met. Since NDE techniques allow us to investigate the microstructure of materials, material damage can be detected at an early stage before macroscopic defects occur. This capability of NDE can help to secure the structural integrity of critical parts to maintain safe and effective operation of aging infrastructure, while reducing maintenance costs.

1.1.1 Nonlinear Ultrasound and Second Harmonic Generation Techniques

The benefit of nonlinear ultrasound compared to linear ultrasound is the ability of interacting with the material's microstructure, which is orders of magnitude smaller than the ultrasonic wavelength [1]. Therefore, nonlinear ultrasound is appropriate for the detection of microscopic damage before macroscopic defects like cracks develop and grow to a critical size. The second harmonic generation (SHG) measurement method is a subset of nonlinear ultrasonic NDE techniques and was developed in the 1960s. This method utilizes the interaction of a monochromatic wave with the microstructure of a solid material, in which it propagates. Through this interaction with dislocations, precipitates and microcracks, that cause nonlinearity, a second harmonic wave is generated. Thus, SHG measurements are capable of detecting microscopic defects in the material resulting from thermal aging, creep, fatigue, corrosion, and

radiation damage. By measuring the amplitudes of the first (A_1) and second (A_2) harmonic wave, the acoustic nonlinearity parameter β can be calculated. This β quantifies the nonlinearity of the material and hence, the materials' microstructural transformations. For a more detailed overview of SHG theory and methods, the author recommends [1].

1.1.2 Micromechanics Models

There exist different micromechanical models to describe solids containing microscopic cracks between thin material layers. These microcracks result in a nonlinear stress-strain relationship and consequently in the generation of higher harmonics in propagating monochromatic waves. The foundation for successful application of NDE techniques to materials with microcracks relies on a global understanding and mathematically detailed description of the interaction between microcracks and ultrasonic waves. Hence, the derivation of a relationship between the acoustic nonlinearity parameter β and material parameters, such as crack density is of high importance.

A general review on modeling the influence of microcracks on the mechanical behavior can be found in [2]. Different models of crack-induced nonlinearity in propagating monochromatic waves are reviewed in [3]. These models can be divided into three major classes based on their concept. The first category includes models based on bilinear stiffness. This approach was presented in 1976 by Budiansky and O'Connell based on the Eshelby method [4]. Extensions of this model and the corresponding calculation of the effective elastic properties can be found in Horii and Nemat-Nasser [5] and Kachanov [6], [7]. The Bilinear Stiffness model proposed by Zhao et al. [8] will be explained briefly in section 4.1. A second category contains models building on rough surface contact. In this context, Buck et al. [9] presented an experimental study in 1978. Followed by a corresponding theoretical examination of Richardson [10] in 1979. Another mechanism is described by Solodov [11]. In 1997 Nazarov and

Sutin [12] published a crack model that was developed by applying methods from elastic contact mechanics to cracks with rough surfaces. The Rough Surface Contact model from Nazarov and Sutin will be described shortly in section 4.2. Cantrell carried out further examinations based on the Nazarov and Sutin model in [13] and [14]. Oberhardt et al. [15] and Rjelka et al. [16] carried out finite element simulations on models based on contact mechanics. The third category incorporates models based on hysteretic material behavior. Guyer and Johnson for instance presented such an approach in [17].

In recent research from Hoffmann et al. [18] a new micromechanics model for materials with aligned microcracks was derived. Hoffmann's model is based on a combination of the Bilinear Stiffness model from Zhao et al. [8] and the Rough Surface Contact model from Nazarov and Sutin [12] for a more comprehensive description of the mechanical behavior of materials containing aligned microcracks. Since this thesis builds on the research from Hoffmann et al. a more detailed description of the combined model approach is presented in chapter 5.

1.1.3 Application - Nanostructured Ferritic Alloys (NFA)

This research addresses materials containing microcracks aligned in one spatial direction, leading to a layer-like materials' structure. These layer-like structures can result from mechanical processing and to name a specific material, nanostructured ferritic alloys (NFAs) are considered in this context. The development of NFAs and the corresponding research on material properties has made significant process throughout the last decade. Publications from Odette et al. [19], [20] and Kim et al. [21] present the current state of progress. The following passage summarizes their papers for a brief introduction on NFAs.

NFAs consist of an iron-chromium-based ferritic stainless steel with a very high contingent of Y-Ti-O rich nano-oxides. The nano-oxide inclusions enable the follow-

ing overall material properties: They repress dislocation travel, stabilize the grain and dislocation formations and, therefore, increase the alloy's strength. Further, the nano-oxides trap helium from irradiation influence, since small high-pressure gas bubbles at the interface between the nano-oxides and the ferritic matrix are formed. This property controls the helium transport and supports stabilization and recombination of the helium. Further characteristics of NFAs are small grain sizes and high dislocation densities, which enable NFAs several high-performance properties. Depending on the performed heat treatment NFAs have high tensile strengths ranging from 600 to 1600 MPa. They provide thermal stability up to temperatures of 1000 °C and retain high creep and fatigue strengths over a wide range of temperatures. The high irradation tolerance, especially under exposure to helium is another key characteristic of NFAs.

These characteristics make NFAs a promising material for advanced fission and fusion applications where preservation of the structural integrity is essential. Therefore, the study and comprehensive understanding of possible damage mechanisms in NFAs is of high importance. Their layer-like and highly anisotropic structure of mechanically processed NFAs typically result from rolling throughout the manufacturing process. This leads to a structure with the most brittle and least stiff direction perpendicular to the layers. Figure 1.1 schematically shows the microstructure, cracks and delaminations of NFAs. The parallel arrangement of the cracks is depicted in figure 1.2, which illustrates a scanning electron microscope image of microcracks in a NFA specimen.

1.2 Objective

The objective of this research is to derive a relationship of the acoustic nonlinearity parameter β - which is defined in the following chapter - in dependence of crack parameters, such as crack radius or number of cracks per volume for the combined

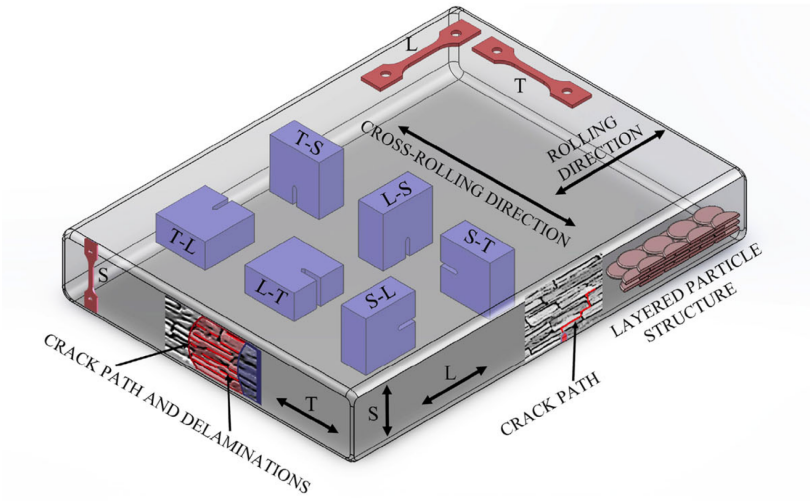

Figure 1.1: Schematic microstructure of NFAs [20]

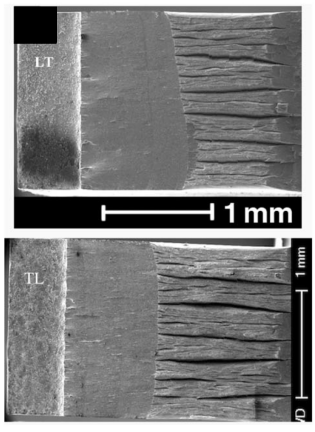

Figure 1.2: Scanning electron microscope image of NFA specimen [20]

micromechanical model for materials with aligned microcracks from Hoffmann et al. [18]. Therefore, the nonlinear, hyperbolic wave equation proposed by Hoffmann et al. has to be solved for varying material input parameters. This investigation is carried out numerically utilizing a high-resolution, semi-discrete numerical solver.

1.3 Outline

In chapter 2, a brief introduction to linear and nonlinear wave propagation is given. Chapter 3 presents a summary of Hoffmann's research with an emphasis placed on the derivation of the nonlinear, hyperbolic wave equation. Followed by chapter 4, which introduces some general theory of hyperbolic partial differential equations and of systems of conservation laws. The applied numerical schemes and corresponding characteristics of these schemes are stated in chapter 5. Chapter 6 presents the consulted simulation parameters shortly and discusses the numerical results. Based on the discussion of the results a relationship for β is derived in this section as well. Finally, chapter 6 completes this thesis with a conclusion and an outlook on possible future work.

CHAPTER 2
WAVE PROPAGATION

This thesis investigates the propagation of plane monochromatic longitudinal waves in elastic solid materials in 1-D. In this context, monochromatic connotes that the considered waves oscillate only with a single constant circular frequency ω. In longitudinal plane waves the displacements only vary in propagation direction and therefore, all wavefronts are parallel. That also means that the amplitude vector of the oscillation is parallel to the propagation direction. This thesis and the underlying research from Hoffmann et al. [18] do not take other physical effects, such as dissipation, scattering and diffraction into consideration. All the subsequent derivations and explanations only consider the one-dimensional case.

2.1 Linear Wave Propagation

This section on the general concepts of linear wave propagation and the derivation of the linear wave equation is predicated on [22] and [23]. A common procedure for the derivation of the linear wave equation is to consider a thin, homogeneous rod with constant density ρ. Figure 2.1 shows an infinitesimal volume element dV of the rod under the exposure of a stress field $\sigma(x,t)$. The corresponding length of the volume element is denoted by dx where the x-axis represents the longitudinal axis of the rod. The applied stress field $\sigma(x,t)$ and thus the resulting displacements $u(x,t)$ can vary in time t and along the longitudinal direction x, but remain constant over the cross-section A, which itself stays constant over the whole rod.

In the absence of body forces and by utilizing a first-order Taylor series expansion for small dx (linearization), the resulting equation of motion along the x-direction

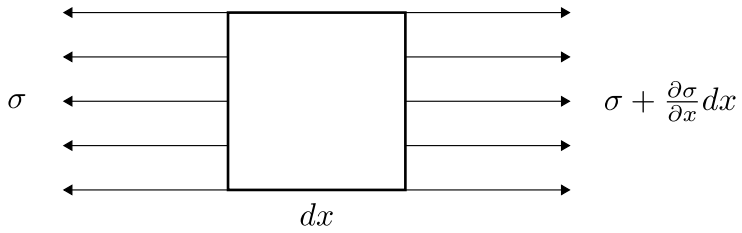

Figure 2.1: Infinitesimal volume element dV of a rod exposed to a stress field $\sigma(x,t)$

yields

$$\rho A dx \frac{\partial^2 u}{\partial t^2} = -\sigma A + (\sigma + \frac{\partial \sigma}{\partial x} dx) A. \tag{2.1}$$

With the assumptions of constant cross-sections A along the whole rod equation 2.1 reduces to

$$\rho \frac{\partial^2 u}{\partial t^2} = \frac{\partial \sigma}{\partial x}. \tag{2.2}$$

Introducing the following constitutive equation, also known as Hooke's law,

$$\sigma = E\varepsilon = E \frac{\partial u}{\partial x} \tag{2.3}$$

and plugging it into the wave equation 2.2, states the below-mentioned equation, which is now only valid for linear elastic solids

$$\rho \frac{\partial^2 u}{\partial t^2} = \frac{\partial}{\partial x}(E \frac{\partial u}{\partial x}). \tag{2.4}$$

The assumption of homogeneity leads to a constant Young's modulus E and therefore, by introducing the longitudinal wave velocity (phase velocity) $c_L^2 = E/\rho$ the linear wave equation results in

$$\frac{\partial^2 u}{\partial t^2} = c_L^2 \frac{\partial^2 u}{\partial x^2}. \tag{2.5}$$

The following displacement wave displays a harmonic solution to linear wave equation

$$u(x,t) = A cos(\omega(\tfrac{x}{c_L} - t)), \tag{2.6}$$

where A is the displacement amplitude and ω the circular frequency. A common physical quantity, which is used to describe waves refers to the wave number k. The wave number is related as follows to the circular frequency ω, the wavelength λ, and the period T:

$$k = \frac{\omega}{c_L} = \frac{2\pi}{\lambda} \qquad with \qquad \omega = \frac{2\pi}{T}. \tag{2.7}$$

Therefore, equation 2.6 can be rewritten to

$$u(x,t) = Acos(kx - \omega t). \tag{2.8}$$

For mathematical convenience, the complex notation of equation 2.8 is oftentimes utilized

$$u(x,t) = Ae^{i(kx-\omega t)} = A(cos(kx - \omega t) + isin(kx - \omega t), \tag{2.9}$$

where the real or imaginary parts represent the physical solution.

2.2 Nonlinear Wave Propagation

By applying Hooke's law in the previous section the resulting wave equation 3.11 represented only linear material behavior, i.e. only waves of the same circular frequency ω as the excitation frequency ω can appear in the material. However, for materials with nonlinear constitutive equations, the medium generates higher harmonic waves. These higher harmonic waves and their related frequencies are integer multiples of the excitation frequency. A conceptual display of the higher harmonics generation in nonlinear media compared to linear media is presented in figure 2.2. The origin of nonlinearity can be caused differently for various materials due to precipitates, dislocations, or microcracks. The subsequent section is based on [1].

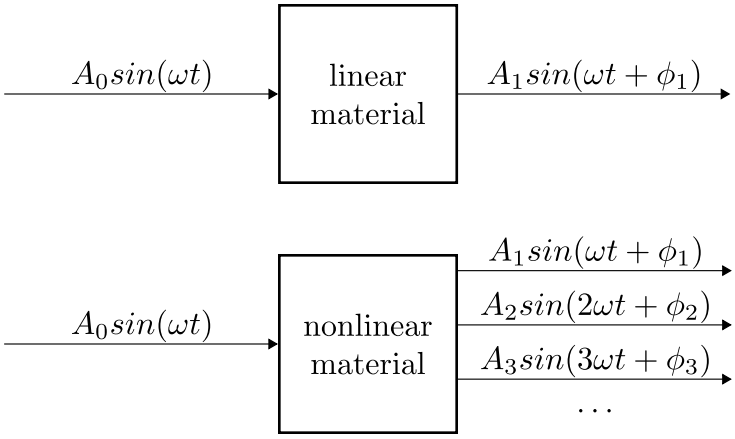

Figure 2.2: Higher harmonics generation of nonlinear media compared to linear media

The constitutive equation for a material with quadratic nonlinearity reads

$$\sigma = \sigma_0 + E_1 \frac{\partial u}{\partial x} + \frac{1}{2} E_2 (\frac{\partial u}{\partial x})^2, \tag{2.10}$$

with σ_0 denoting the initial stress and E_1 and E_2 representing the second- and third-order elastic constants of the material. Applying this nonlinear constitutive relationship 2.10 to the universal equation of motion 2.2 yields the nonlinear wave equation for longitudinal waves in 1-D

$$\frac{\partial^2 u}{\partial t^2} = c_L^2 (1 - \beta \frac{\partial u}{\partial x}) \frac{\partial^2 u}{\partial x^2} \tag{2.11}$$

where β denotes the acoustic nonlinearity parameter. The derivation of equation 2.11 introduces the general expression of β in terms of elastic constant as

$$\beta = -\frac{E_2}{E_1}. \tag{2.12}$$

The harmonic solution to equation 2.11 has the form

$$u(x,t) = A_1 sin(kx - \omega t) + \frac{\beta A_1^2 x k^2}{8} cos(2kx - 2\omega t) + ... \tag{2.13}$$

containing higher harmonic frequencies $2\omega, 3\omega$ etc., other than the linear case. The amplitude of the first harmonic is A_1 and from equation 2.13 the amplitude of the second harmonic A_2 can be found as

$$A_2 = \frac{\beta A_1^2 x k^2}{8} = \frac{\beta A_1^2 x \omega^2}{8 c_L^2}. \tag{2.14}$$

Reversely, the acoustic nonlinearity parameter β can be determined

$$\beta = \frac{8 A_2}{A_1^2 x k^2} = \frac{8 A_2 c_L^2}{A_1^2 \omega^2 x}. \tag{2.15}$$

This expression shows that β is related to the amplitudes A_1 and A_2 of the first and second harmonic amplitude, to the wavenumber k of the propagating wave and the propagation distance x. As a consequence, by measuring all these parameters one can determine the acoustic nonlinearity β. Moreover, equation 2.15 states that β is proportional to A_2/A_1^2 for longitudinal plane waves propagating in isotropic materials with quadratic nonlinearity. The generation of a second harmonic wave means that energy is transferred from the first to the second harmonic. This effect is oftentimes neglected in literature, since the energy loss of A_1 is much smaller than the overall energy of the first harmonic wave for small propagation distances. In addition, the amplitude A_2 is magnitudes smaller compared to the amplitude A_1. The presented derivation of the acoustic nonlinearity parameter β can be dilated and adjusted to three spatial dimensions and special types of waves, such as Rayleigh and Lamb waves as well.

CHAPTER 3
BACKGROUND - COMBINED MICROMECHANICS MODEL

As mentioned in chapter 1, various models on the description of micromechanical structures for solids containing microcracks exist. While most of the existing publications only focus on a single microcrack modeling approach, Hoffmann et al. [18],[24] recently combined the Bilinear Stiffness model of Zhao et al. [8] and the Rough Surface Contact model from Nazarov and Sutin [12] to a more comprehensive model for aligned microcracks. This chapter gives a brief summary of the research from Hoffmann et al. focusing on their derivation of the nonlinear stress-strain relationship for the combined model and the resulting nonlinear, hyperbolic wave equation.

3.1 Bilinear Stiffness Model

One of the underlying models for Hoffmann's research is the Bilinear Stiffness model from Zhao et al. [8]. It assumes that all cracks in the solid are open under external tensional loads, which result in a reduced stiffness and therefore, a reduced effective Young's modulus $E_t < E$. However, under external compressional loads the model supposes all cracks to be closed. The effective Young's modulus $E_c = E$ remains unchanged as if the solid did not contain cracks. This conservation of the Young's modulus in the compressive case only holds for longitudinal waves propagating normally to the crack, which is an underlying assumption of Hoffmann's research. A conceptual display of the stress-strain relationship for the Bilinear Stiffness model is shown in figure 3.1.

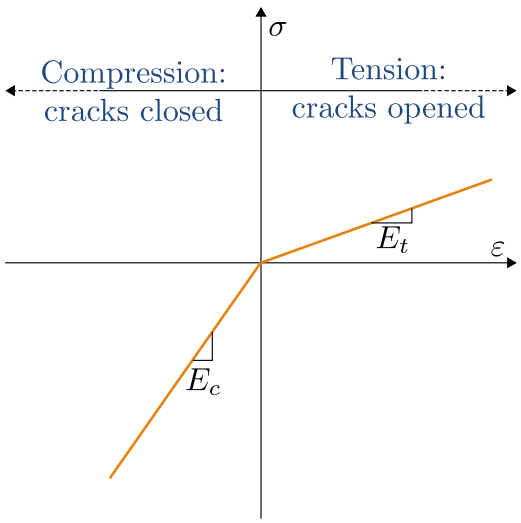

Figure 3.1: Schematic stress-strain relationship based on a bilinear stiffness approach

3.2 Rough Surface Contact Model

The other fundamental model in Hoffmann's research constitutes the Rough Surface Contact model from Nazarov and Sutin [12]. In this model the cracks are never completely closed or opened. Rather, Nazarov and Sutin assume that the rough crack faces always stay in elastic contact to each other; pressed together by internal stresses from the surrounding material. As a result, the asperities deform depending on the variation of the superimposed normal stress from a longitudinal wave traveling perpendicular to the cracks.

3.3 Combined Model

3.3.1 Main Idea

Depending on the applied external loads one can easily imagine that both, the Bilinear Stiffness model and the Rough Surface Contact model, have to be taken into account for representing the materials' behavior. Therefore, three different stages can occur: For large compressive loads the cracks are closed and the effective Young's modulus

Table 3.1: Numerical material parameters for NFAs [18]

Symbol	Value	Explanation
E	190 GPa	Young's modulus of the uncracked material
ν	0.25	Poisson's ratio of the uncracked material
R	$0.5 \cdot 10^{-3}$ m	crack radius
N_0	$3 \cdot 10^{8}$ m	number of cracks per m^3
h_S	10^{-8} m	$\sqrt{2}$times effective height of roughness
a	$2 \cdot 10-4$ m	radius of conical asperity
d_0	$3 \cdot 10^{-8}$ m	initial distance between crack faces
x	$8.509 \cdot 10^{-3}$ m	thickness of specimen
c_L	5972 m/s	longitudinal wave velocity

$E_c = E$ applies to the material. In contrast, for large tensile loads the cracks are completely opened and the reduced effective Young's modulus E_t from the Bilinear Stiffness model is representative. However, under small tensile and compressive loads the asperities will remain in contact and the cracks are only partially closed/opened.

3.3.2 Numerical Values of Material Properties

For the derivation of the combined model Hoffmann et al. supports the general procedure with a numerical example for the considered NFA material. These values are stated in table 3.1.

3.3.3 Acoustic Nonlinearity Parameter β

As mentioned in section 1.1.2 the derivation of a relationship between the acoustic nonlinearity parameter β and material parameters is crucial for the successful application of NDE techniques. Equation 3.1 depicts the definition of the acoustic

nonlinearity parameter β for the Bilinear Stiffness model from Zhao et al. [8]

$$\beta = \frac{3\pi c_L A_2}{A_1 \omega x} \equiv \beta_B. \tag{3.1}$$

The important information we gather from this equation is that the amplitude of the second harmonic A_2 is proportional to the one of the first harmonic A_1. Recalling equation 2.15, we see that the definition of β in the Bilinear Stiffness model differs from the usual definition for uncracked solid materials, where A_2^2 is proportional to A_1.

Nazarov and Sutin [12] derived the acoustic nonlinearity parameter β as follows starting with the nonlinear stress-strain relationship

$$\sigma(\varepsilon) = EG_1 \left(\varepsilon - \frac{G_2}{2}\varepsilon^2 - \frac{G_3}{6}\varepsilon^3 \right) \tag{3.2}$$

. In the following Hoffmann et al. neglected the third-order term $(G_3/6)\varepsilon^3$ since their research focuses on second harmonic generation due to quadratic nonlinearity. Additionally, simulations have shown that neglecting the third-order term is valid for sufficiently small ε, where the Rough Surface Contact model applies. See [24] for detailed information. This leads to a second-order nonlinear stress-strain relationship

$$\sigma(\varepsilon) = EG_1 \left(\varepsilon - \frac{G_2}{2}\varepsilon^2 \right) \tag{3.3}$$

of the same form as 2.10. The comparison of both equations 3.3 and 2.10 points out that the coefficients G_i are related to the elastic constants E_i by $E_1 = EG_1$ and $E_2 = -EG_1G_2$. Since chapter 2 proved that plugging the general second-order nonlinear constitutive relationship 2.10 into the universal equation of motion 2.2 results in the general term 2.12 for β, the mentioned comparison shows that the acoustic nonlinearity parameter for the Rough Surface Contact model from Nazarov

and Sutin is denoted by $\beta = G_2$. In terms of crack parameters the written out expression for G_2 reads

$$G_2 = \frac{N_0 R^4 h_s (16\nu^2 - 16)^2}{9 d_0^2 \pi \frac{N_0 R^3 h_s (16\nu^2 - 16)}{3 d_0 (h_s/d_0 + 1) - 1})^2 (h_s/d_0 + 1)^3} \equiv \beta_{RSC}. \tag{3.4}$$

The term G_1 expressed in terms of crack parameters reads

$$G_1 = -\left(\frac{N_0 R^3 h_s (16\nu^2 - 16)}{3 d_0 (h_s/d_0 + 1) - 1} \right)^{-1}. \tag{3.5}$$

Because equation 2.12 holds for the Rough Surface Contact model, it relates the first and second harmonic amplitudes in the same way as the usual definition 2.15, where A_2 is proportional to A_1^2.

This leads to different definitions of the acoustic nonlinearity parameter β for the presented Bilinear Stiffness model and the Rough Surface Contact model, and thus, the derivation of such a relationship for a combined model becomes nontrivial. As a consequence, Hoffmann et al. utilized micromechanical modeling tools to derive a more comprehensive model resulting in an overall stress-strain where tension, compression and asperity contact of the cracked solid are incorporated. Figure 7.1 depicts the schematical overall stress-strain relationship containing the three described ranges.

3.3.4 Transitions ε_1 and ε_2

As can be seen in figure 7.1 the strains ε_1 and ε_2 with their corresponding stresses denote the transitions between completely opened cracks, asperity contact, and closed cracks. Referring to Hoffmann et al. the transitions are identified by matching the slopes of the Bilinear Stiffness model with the slope of the quadratic nonlinear stress-strain relationship 3.3. To ensure additionally, that not only the slopes of both models match, but also their stress values at the transitions, the Bilinear Stiffness model

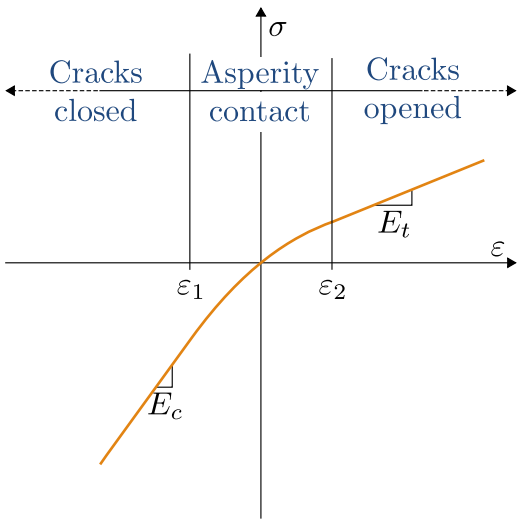

Figure 3.2: Schematic of the overall nonlinear stess-strain relationship of the combined model adapted from [18]

had to be shifted. This procedure fully defines the second-order, nonlinear, stress-strain relationship of the combined model. Furthermore, it leads to a dependence between the transitions ε_1, ε_2, and the acoustic nonlinearity parameter $G_2(\beta_{RSC})$ of the Rough Surface Contact model and therefore, the transitions are related to the material parameters N_0, R,h_S, ν, and d_0. This relationship can be expressed as follows based on the procedure described above

$$\varepsilon_1 = \frac{EG_1 - E_c}{EG_1G_2} \quad and \quad \varepsilon_2 = \frac{EG_1 - E_t}{EG_1G_2}. \tag{3.6}$$

For the material parameters proposed by Hoffmann et al. the transitions yield $\varepsilon_1 = -7.345 \cdot 10^{-5}$, $\varepsilon_2 = 1.856 \cdot 10^{-4}$.

3.3.5 Nonlinear Stress-Strain Relationship and Resulting Wave Equation

According to Hoffmann et al. the resulting overall stress-strain relationship is defined as

$$\begin{aligned}\sigma(\varepsilon) =&(E_c H[-(\varepsilon-\varepsilon_1)] + E_a(H[\varepsilon-\varepsilon_1] - H[\varepsilon-\varepsilon_2]) + E_t H[\varepsilon-\varepsilon_2])\varepsilon \\ &- \tfrac{1}{2}E_a G_2 \varepsilon^2 (H[\varepsilon-\varepsilon_1] - H[\varepsilon-\varepsilon_2]) \\ &+ H[-(\varepsilon-\varepsilon_1)]((E_a - E_c)\varepsilon_1 - \tfrac{1}{2}E_a G_2 \varepsilon_1^2) \\ &+ H[\varepsilon-\varepsilon_2]((E_a - E_t)\varepsilon_2 - \tfrac{1}{2}E_a G_2 \varepsilon_2^2)\end{aligned} \tag{3.7}$$

where H denotes the Heaviside step function and the quantity $E_a = EG_1$ results from the Rough Surface Contact model.

The first line of equation 3.7 represents the different slopes of the linear parts. The second line originates from the quadratic nonlinearity of the Rough Surface Contact model and the last two lines specify the necessary shifts of the bilinear parts for combining both underlying models. By implementing $H[-x] = 1 - H[x]$ and introducing the relative quantities

$$\gamma_c = \frac{E_c - E_a}{E_c}, \qquad \gamma_t = \frac{E_t - E_a}{E_c} \tag{3.8}$$

equation 3.7 can be transformed into

$$\begin{aligned}\sigma(\varepsilon) =&E_c(1 - \gamma_c H[\varepsilon-\varepsilon_1] + \gamma_t H[\varepsilon-\varepsilon_2])\varepsilon \\ &+ E_c(-\gamma_c\varepsilon_1 + \gamma_c H[\varepsilon-\varepsilon_1]\varepsilon_1 - \gamma_t H[\varepsilon-\varepsilon_2]\varepsilon_2) \\ &+ \tfrac{1}{2}E_a G_2(H[\varepsilon-\varepsilon_2](\varepsilon^2 - \varepsilon_2^2) - H[\varepsilon-\varepsilon_1](\varepsilon^2 - \varepsilon_1^2) - \varepsilon_1^2).\end{aligned} \tag{3.9}$$

For investigation of the interaction between the above standing nonlinear stress-strain

relationship and ultrasonic waves, the derivative of equation 3.9 was calculated

$$\begin{aligned}\frac{\partial \sigma}{\partial x} =& E_c \frac{\partial^2 u}{\partial x^2} - E_c(\gamma_c H[\frac{\partial u}{\partial x} - \varepsilon_1] - \gamma_t H[\frac{\partial u}{\partial x} - \varepsilon_2])\frac{\partial^2 u}{\partial x^2} \\ & - E_a G_2(H[\frac{\partial u}{\partial x} - \varepsilon_1] - H[\frac{\partial u}{\partial x} - \varepsilon_2])\frac{\partial u}{\partial x}\frac{\partial^2 u}{\partial x^2}.\end{aligned} \tag{3.10}$$

As a final step equation 3.10 was plugged into the wave equation. Utilizing the property of the Dirac delta function $x\delta(x) = 0$ yields

$$\frac{\partial^2 u}{\partial t^2} - c_{L,c}^2 \frac{\partial^2 u}{\partial x^2} = -c_{L,c}^2(\gamma_c f_c(u) - \gamma_t f_t(u)) - c_{L,c}^2 \gamma_a (f_{q,c}(u) - f_{q,t}(u)) \tag{3.11}$$

The longitudinal wave velocity $c_{L,c}^2 = \frac{E_c}{\rho}$ is defined based on the effective compressive Young's modulus E_c and $\gamma_a = \frac{E_a G_2}{E_c}$ is introduced as an abbreviation. Furthermore, the following auxiliary functions were defined for convenience

$$\begin{aligned} f_c(u) &= H[\frac{\partial u}{\partial x} - \varepsilon_1]\frac{\partial^2 u}{\partial x^2}, \qquad f_t(u) = H[\frac{\partial u}{\partial x} - \varepsilon_2]\frac{\partial^2 u}{\partial x^2}, \\ f_{q,c}(u) &= H[\frac{\partial u}{\partial x} - \varepsilon_1]\frac{\partial u}{\partial x}\frac{\partial^2 u}{\partial x^2}, \qquad f_{q,t}(u) = H[\frac{\partial u}{\partial x} - \varepsilon_2]\frac{\partial u}{\partial x}\frac{\partial^2 u}{\partial x^2}. \end{aligned} \tag{3.12}$$

3.3.6 Pertubation Approach

Hoffmann et al. approximated the solution of the resulting nonlinear wave equation 3.11 using the pertubation method. The pertubation method assumes that the overall solution for the total displacement field u can be split up into $u = u_1 + u_2$ consisting of the known solution u_1 to the linear wave equation and higher order pertubations u_2. Therefore, after decomposing the overall partial differential equation, in a first step u_1 is determined. As a second step, u_1 is plugged into the remaining partial differential equation for u_2 and acts as a pertubation term. The entire derivation can be found

in [18]. This pertubation approach generally only holds if $|u_2| << |u_1|$, which is oftentimes the case for second harmonic generation problem. In the context of the NFA material under consideration, this assumption and therefore, the pertubation method does not provide an appropriate solution approximation anymore. This is due to the high quadratic nonlinearity $\beta_R SC = G_2 = 638.18$ resulting from the chosen material parameters in 3.1. As a consequence, the nonlinear wave equation 3.11 has to be solved by consulting appropriate numerical methods, which is the objective of this research. The following chapter presents some mathematical concepts behind equation of the same structure as 3.11, so called hyperbolic partial differential equations before chapter 5 introduces numerical schemes.

CHAPTER 4
THEORY OF HYPERBOLIC PARTIAL DIFFERENTIAL EQUATIONS

Partial differential equations can be used to model a broad variety of fundamental laws of nature. They range from acoustics, heat transfer, electrodynamics, fluid dynamics, quantum mechanics to solid mechanics. A common classification for second-order linear partial differential equations is the separation into parabolic, hyperbolic and elliptic equations. This classification, in general, is not possible for all second-order linear partial differential equation, since it depends on the particular domain the equations are examined in. For a more detailed treatment of partial differential equations and their classification the author recommends [25].

This thesis focusses on nonlinear hyperbolic partial differential equations, which oftentimes relate to wave propagation and advective transport phenomena. Therefore, a brief introduction on the basic theoretical concepts of hyperbolic partial differential equations is given in this chapter. First of all, scalar partial differential equations are considered in order to present general solution concepts. Thereafter, systems of partial differential equations and their corresponding solution dynamics are examined. In the last part, the emphasis is put on the conservation formulation of systems of hyperbolic partial differential equations, which are used in this thesis for solving the governing problem. For a more detailed and complete view, the author recommends the theoretical chapters of [5], [32], [7], [25], and [27]. In the following chapters a common notation for partial derivatives is used $u_t = \frac{\partial u}{\partial t}$ and $u_x = \frac{\partial u}{\partial x}$.

4.1 Scalar Hyperbolic Equations

All explanations and derivations in this section are based on the following quasi-linear form of a one-dimensional, scalar, hyperbolic partial differential equation

$$\frac{\partial u}{\partial t} + c(u)\frac{\partial u}{\partial x} = 0, \quad x \,\epsilon\, \mathbb{R}, \quad t > 0. \tag{4.1}$$

The term quasi-linear is specified in chapter 4.2.1 in the context of systems of partial differential equations as well as a definition of hyperbolicity. Equation 4.1 can be utilized for obtaining an insight into the solution dynamics for continuous solutions as well as the development of shock waves. A general approach for this purpose is the method of characteristics, which is briefly introduced in the following. The total derivative with respect to time t of $u(x,t)$ on an arbitrary curve $x = x(t)$ in the x-t-plane reads

$$\frac{du}{dt} = \frac{\partial u}{\partial t} + \frac{dx}{dt}\frac{\partial u}{\partial x}. \tag{4.2}$$

By renaming the slope of this curve

$$\frac{dx}{dt} = c(u) \tag{4.3}$$

and comparing equation 4.2 to the original equation 4.1 leads to

$$\frac{du}{dt} = 0 \qquad \Rightarrow \qquad u = u_0 = constant. \tag{4.4}$$

The slope 4.3 represents the local wave speed and the curves defined by it are called characteristics of equation 4.1. Since equation 4.4 shows that u is constant, it follows that $c(u)$ is constant as well and the characteristics become straight lines in the x-t-plane. Straight characteristic lines only appear in the quasi-linear case, which is not the general case.

The solution to equation 4.1 can be determined by applying smooth initial data of the form

$$u(x, t = 0) = g(x), \qquad -\infty < x < \infty. \tag{4.5}$$

With the property of a constant solution along characteristic lines, a solution

$$u = g(\zeta_0) \tag{4.6}$$

is represented by the characteristic passing through $x = \zeta_0$ at $t = 0$

$$x = \zeta_0 + G(\zeta_0)t \tag{4.7}$$

where $G(\zeta_0) = c(g(\zeta_0))$ denotes the slope of the characteristic. The family of solutions for all x is obtained by varying ζ

$$u = g(\zeta) \qquad with \qquad c(g(\zeta)) = G(\zeta) \tag{4.8}$$

on the characteristics

$$x = \zeta + G(\zeta)t. \tag{4.9}$$

By calculating the partial derivatives of our proposed solution u, one can easily check if this implicit solution given by equations 4.8 and 4.9 is the solution to the governing equation 4.1

$$u_t = g'(\zeta)\zeta_t, \qquad u_x = g'(\zeta)\zeta_x \tag{4.10}$$

and

$$0 = (1 + G'(\zeta)t)\zeta_t + G(\zeta), \qquad 1 = (1 + G'(\zeta)t)\zeta_x. \tag{4.11}$$

Combining 4.10 and 4.11, we receive

$$u_t = -\frac{G(\zeta)g'(\zeta)}{1+G'(\zeta)t}, \qquad u_x = \frac{g'(\zeta)}{1+G'(\zeta)t} \tag{4.12}$$

and it can be seen that equation 4.12 satisfies equation 4.1, since $G(\zeta) = c(u)$. Besides the presented solution for smooth initial data with a constant local wave speed $c(u)$, the above derived equations can be utilized for further investigation of the solution dynamics. For hyperbolic equations, this investigation covers the development of shock waves and rarefaction waves, which is presented in detail in [26], [27], and [28].

4.2 Systems of Hyperbolic Equations

In this section systems of hyperbolic partial differential equations are introduced. Only one-dimensional systems with a single spatial coordinate x are considered in order to familiarize with the main concepts and properties. An extension to higher-dimensional systems can be found in [28].

4.2.1 System Classification

The following classification of first-order partial differential equations in one dimension is based on [25] and [28]. Starting from the most general, first-order system of partial differential equations in one dimension

$$\boldsymbol{F}(x, t, \boldsymbol{u}, \boldsymbol{u}_x, \boldsymbol{u}_t) = 0, \qquad \boldsymbol{u} \,\epsilon\, \mathbb{R}^P \tag{4.13}$$

where $\boldsymbol{F}$ is a given function and $\boldsymbol{u} = \boldsymbol{u}(x,t)$ is an unknown function of the independent variables x and t, denoting the spatial variable and time in this thesis, respectively. Equation 4.13 is called a **nonlinear** system of partial differential equations. In the case that equation 4.13 is linear in its partial derivatives of $\boldsymbol{u}(x,t)$ the system is named

quasi-linear system and has the form

$$\boldsymbol{A}(x,t,\boldsymbol{u})\boldsymbol{u}_t + \boldsymbol{B}(x,t,\boldsymbol{u})\boldsymbol{u}_x + \boldsymbol{c}(x,t,\boldsymbol{u}) = 0, \qquad \boldsymbol{u} \in \mathbb{R}^P. \tag{4.14}$$

Furthermore, if the coefficient matrices $\boldsymbol{A}$ and $\boldsymbol{B}$ are independent of the unknown function $\boldsymbol{u}(x,t)$ the system is denoted as a **semi-linear** system of partial differential equations possessing the following structure

$$\boldsymbol{A}(x,t)\boldsymbol{u}_t + \boldsymbol{B}(x,t)\boldsymbol{u}_x + \boldsymbol{c}(x,t,\boldsymbol{u}) = 0, \qquad \boldsymbol{u} \in \mathbb{R}^P. \tag{4.15}$$

In the case, where $\boldsymbol{F}$ is linear in each variable $\boldsymbol{u}$, $\boldsymbol{u}_x$, and $\boldsymbol{u}_t$ and the coefficient matrices are only functions of the independent variables x and t, the system is called **linear** system of partial differential equations and can be expressed as

$$\boldsymbol{A}(x,t)\boldsymbol{u}_t + \boldsymbol{B}(x,t)\boldsymbol{u}_x + \boldsymbol{C}(x,t)\boldsymbol{u} + \boldsymbol{d}(x,t) = 0, \qquad \boldsymbol{u} \in \mathbb{R}^P. \tag{4.16}$$

Equation 4.16 depicts the most general, first-order linear system of partial differential equations. The coefficient matrices $\boldsymbol{A}$, $\boldsymbol{B}$, and $\boldsymbol{C}$ are now only dependent of x and t.

In the case, when vector $\boldsymbol{d}(x,t) \equiv \boldsymbol{0}$ equals the zero-vector, equation 4.16 is denoted as homogeneous. Otherwise equation 4.16 is an inhomogeneous linear system of partial differential equations.

4.2.2 Hyperbolicity and Characteristics

The subsequent definition of hyperbolicity builds on the general form of a first-order, quasi-linear equation 4.1 and follows the procedure in [27]. It utilizes the Einstein notation, i.e. summation over the repeated index. As we proved in the previous section, the solution to a hyperbolic, quasi-linear partial differential equation can be represented by a family of characteristics. Along each characteristic the partial

differential equation can be reduced to an ordinary differential equation allowing to solve the overall problem by solving the ordinary differential equations for all characteristics. This idea breaks the governing problem down into local problems over small regions and is based on the presumption of finite propagation speed, which means that the behavior at a point in any small time increment can be influenced only by points near enough for their waves to arrive in time. To answer the question about hyperbolicity, we need to prove that such local calculations are possible. Therefore, we start with the following linear combination of equation 4.1 for each u_j

$$l_i(A_{ij}\frac{\partial u_j}{\partial t} + B_{ij}\frac{\partial u_j}{\partial x}) + l_i c_i = 0. \tag{4.17}$$

Vector $\boldsymbol{l}$ is dependent on x, t, $\boldsymbol{u}$ and the task is to check, if $\boldsymbol{l}$ can be chosen, such that equation 4.17 can be transformed into the subsequent form

$$m_j(\beta\frac{\partial u_j}{\partial t} + \alpha\frac{\partial u_j}{\partial x}) + l_j c_j = 0. \tag{4.18}$$

If this transformation is possible, equation **??** provides a relation between the directional derivatives

$$\frac{\partial u_j}{\partial \boldsymbol{q}} = (\nabla u_j)^T \cdot \boldsymbol{q}, \qquad \boldsymbol{q} = [\alpha, \beta]^T \tag{4.19}$$

of all u_j in the single direction $[\alpha, \beta]^T$. Thus, curves in the x-t-plane can be implemented, which are defined by the vector field $[\alpha, \beta]^T$. Introducing the parametric representation of a typical member of this family as $x = X(\eta)$ and $t = T(\eta)$, the total derivative of u_j on the curve results in

$$\frac{du_j}{d\eta} = T'(\eta)\frac{\partial u_j}{\partial t} + X'(\eta)\frac{\partial u_j}{\partial x}. \tag{4.20}$$

Setting $\alpha = X'(\eta)$ and $\beta = T'(\eta)$ equation 4.20 can be transcribed into its characteristic form

$$m_j \frac{du_j}{d\eta} + l_j c_j = 0 \qquad on \qquad \frac{dX}{d\eta} = \alpha,\ \frac{dT}{d\eta} = \beta. \tag{4.21}$$

By specifying the conditions for equation 4.21 in the form of equation **??**

$$l_i A_{ij} = m_j T', \qquad l_i B_{ij} = m_j X' \tag{4.22}$$

we can eliminate m_j and receive

$$l_i (A_{ij} X' - B_{ij} T') = 0. \tag{4.23}$$

Under the following necessary and sufficient condition on the direction of the curve, equation 4.23 provides a nontrivial solution

$$|A_{ij} X' - B_{ij} T'| = 0. \tag{4.24}$$

The above described procedure together with the restriction 4.25 to exclude the degenerate cases, where both coefficient matrices $\boldsymbol{A}$ and $\boldsymbol{B}$ become singular, results in the following definition of **hyperbolicity** [27].

Definition 4.2.1. *A system 4.1, satisfying*

$$|\nu A_{ij} + \mu B_{ij}| \neq 0, \tag{4.25}$$

*for some ν, μ but not both zero, is **hyperbolic** if K linearly independent real vectors $\boldsymbol{l}^{(k)}$, $k = 1, \ldots, K$, can be found such that*

$$\boldsymbol{l}_i^{(k)} \{A_{ij} \alpha^{(k)} - B_{ij} \beta^{(k)}\} = 0 \tag{4.26}$$

for each k, and the corresponding directions $\{\alpha^{(k)}, \beta^{(k)}\}$ *are real with* ${\alpha^{(k)}}^2 + {\beta^{(k)}}^2 \neq 0$.

In this definition the emphasis is placed on the existence of K linearly independent vectors $\boldsymbol{l}^{(k)}$ without necessarily having distinct corresponding directions $\{\alpha^{(k)}, \beta^{(k)}\}$. In the case, where the directions are distinct as well, such that there are K different families of characteristics, the system is called **strictly hyperbolic**.

A special case of equation 4.1 arises in many problems, where the coefficient matrix $\boldsymbol{A}$ equals the unit matrix, such that equation 4.1 reduces to the form

$$\frac{\partial u_i}{\partial t} + B_{ij}\frac{\partial u_j}{\partial x} + c_i = 0. \tag{4.27}$$

Thus, the linear combination 4.17 becomes

$$l_i\frac{\partial u_i}{\partial t} + l_i B_{ij}\frac{\partial u_j}{\partial x} + l_i c_i = 0 \tag{4.28}$$

and the resulting characteristic form is expressed by

$$l_i\frac{du_i}{dt} + l_i c_i = 0 \qquad on \qquad \frac{dX(t)}{dt} = c \tag{4.29}$$

with

$$l_i B_{ij} = l_j c. \tag{4.30}$$

As a consequence, the characteristic velocity c has to satisfy the following equation

$$|B_{ij} - c\delta_{ij}| = 0 \tag{4.31}$$

where c represents the eigenvalues of the coefficient matrix $\boldsymbol{B}$ and $\boldsymbol{l}$ are the left eigenvectors according to equation 4.30. Since the eigenvectors $\boldsymbol{l}$ corresponding to distinct eigenvalues c are linearly independent, *the system 4.27 is hyperbolic if equation 4.31 has K distinct real roots c.*

4.3 Systems of Conservation Laws

Conservation laws represent an important category of equations in the field of partial differential equations, since they can be utilized to model physical phenomena including conserved quantities, like mass, momentum, energy, etc. This research investigates wave propagation problems in continuous elastic media. Such problems are oftentimes described by higher order partial differential equations and can be transformed into conservation law formulation (short: conservation form). This conservation form is of great interest, since various numerical algorithms have been proposed based on the conservation form of systems. In this section a short introduction to systems of conservation laws in one spatial dimension based on [26], [29] is presented. For multiple spatial dimension the author recommends [29].

4.3.1 Integral and Differential Form

The integral form of conservation laws results directly from physical principles by simply formulating the conservation of a particular quantity. Equation 4.32 denotes the **integral form** of conservation laws

$$\int_a^b \boldsymbol{u}(x,t_2)dx - \int_a^b \boldsymbol{u}(x,t_1) = -\left(\int_{t_1}^{t_2} \boldsymbol{f}(\boldsymbol{u}(b,\tau))d\tau - \int_{t_2}^{t_1} \boldsymbol{f}(\boldsymbol{u}(a,\tau))d\tau\right) \tag{4.32}$$

where $\boldsymbol{u} = [u_1, u_2, \ldots, u_K]^T$ is a vector-valued function of conserved quantities depending on x and t, and $\boldsymbol{f} = [f_1, f_2, \ldots, f_K]^T$ are named the **flux functions**. Due to its proximity to the underlying physical principle, the presented integral form allows a physical interpretation in a way that the change of conserved quantities $\boldsymbol{u}$ on the interval $[a, b]$ between times t_1 and t_2 equals the flux of these quantities over the boundaries at $x = a$ and $x = b$ and the time interval $[t_1, t_2]$. Under the assumption that the conserved quantities $\boldsymbol{u}(x,t)$ and their fluxes $\boldsymbol{f}(\boldsymbol{u}(x,t))$ are differentiable the

differential form of conservation laws can be derived. By utilizing

$$\boldsymbol{u}(x,t_2) - \boldsymbol{u}(x,t_1) = \int_{t_1}^{t_2} \frac{\partial}{\partial t}\boldsymbol{u}(x,t)dt \tag{4.33}$$

and

$$\boldsymbol{f}(\boldsymbol{u}(x,t_2)) - \boldsymbol{f}(\boldsymbol{u}(x,t_1)) = \int_{x_1}^{x_2} \frac{\partial}{\partial x}\boldsymbol{f}(\boldsymbol{u}(x,t))dx \tag{4.34}$$

together with equation 4.32 we receive

$$\int_{t_1}^{t_2}\int_{a}^{b} \left\{ \frac{\partial}{\partial t}\boldsymbol{u}(x,t) + \frac{\partial}{\partial x}\boldsymbol{f}(\boldsymbol{u}(x,t)) \right\} dxdt = \boldsymbol{0}. \tag{4.35}$$

From equation 4.35 one can easily deduct that, indeed, the integrand has to equal the zero vector to satisfy the equation for any section $[a,b]$ and time interval $[t_1,t_2]$. This procedure yields

$$\frac{\partial \boldsymbol{u}}{\partial t} + \frac{\partial}{\partial x}\boldsymbol{f}(\boldsymbol{u}) = \boldsymbol{0} \qquad x \,\epsilon\, \mathbb{R}, \qquad t > 0 \tag{4.36}$$

the **differential form** of conservation laws, generally denoted as **conservation form** [30]. The function $\boldsymbol{f(u)}$ is called the **flux function**. The system 4.36 is called **hyperbolic** [29], [30], if the $K \times K$ Jacobian Matrix

$$\boldsymbol{A} = \begin{pmatrix} \frac{\partial f_1}{\partial u_1} & \cdots & \frac{\partial f_1}{\partial u_K} \\ \vdots & & \vdots \\ \frac{\partial f_K}{\partial u_1} & \cdots & \frac{\partial f_K}{\partial u_K} \end{pmatrix} \tag{4.37}$$

has K real eigenvalues

$$\nu_1(\boldsymbol{u}) \leq \nu_2(\boldsymbol{u}) \leq \ldots \nu_K(\boldsymbol{u}) \tag{4.38}$$

and K corresponding linearly independent eigenvectors $\boldsymbol{r}_1(\boldsymbol{u}), \boldsymbol{r}_2(\boldsymbol{u}), \ldots, \boldsymbol{r}_K(\boldsymbol{u})$. If all eigenvalues are not only real, but also distinct, then system 4.36 is denoted as **strictly**

hyperbolic [30].

Furthermore, it is important to mention that for a K system conservation law, K characteristics arise from each point compared to the scalar case, where only one characteristic arises from each point.

4.3.2 Problem Formulations

The solution of partial differential equations demands the specification of variables on the borders of the considered domains. Therefore, initial value, boundary value, and initial-boundary value problem are briefly summarized in this section.

Initial Value Problem

The **initial value problem** (IVP), also known as **Cauchy problem**, for hyperbolic systems based on [29] can be expressed as the search for a function $\boldsymbol{u} : (x,t)\,\epsilon\,\mathbb{R} \times [0,+\infty) \rightarrow \boldsymbol{u}(x,t)$ that represents a solution to equation 4.36 satisfying the initial condition at time $t = 0$

$$\boldsymbol{u}(x,0) = \boldsymbol{u}_0(x), \quad x\,\epsilon\,\mathbb{R} \tag{4.39}$$

with a given function $\boldsymbol{u}_0$.

In the case of discontinuous initial data $\boldsymbol{u}_0$ of the form

$$\boldsymbol{u}_0(x) = \begin{cases} \boldsymbol{u}_L, & x < 0 \\ \boldsymbol{u}_R, & x > 0 \end{cases} \tag{4.40}$$

the Cauchy problem becomes a **Riemann problem** [29],[26],[31]. Riemann problems are of high importance for the development of finite volume methods [31] as well as for so called upwind schemes - a class of finite difference methods for solving hyperbolic partial differential equations. Section 5.12 presents a short introduction to these types of methods, while a more detailed treatment can be found in [30],[29], and [32].

Boundary Value Problem

A boundary value problem (BVP) asks to solve equation 4.36 in a domain Λ with the boundary $\partial\Lambda$ under the condition

$$\boldsymbol{u}(x,t)|_{\partial\Lambda} = \boldsymbol{h}(t) \tag{4.41}$$

with 4.41 denoting the most simple class of boundary conditions. According to [33], even unimpressive appearing BVPs can provide exactly a single solution, no solution at all, or an infinite number of solutions. Therefore, BVPs with randomly prescribed boundary conditions cannot be solved generally and the boundary conditions have significant influence on the well-posedness of the problem. This is why they have to be treated cautious. Nevertheless, for solving conservations laws numerically, the specification of initial as well as boundary conditions is required, leading to initial boundary value problems.

Initial Boundary Value Problem

Finding a solution to equation 4.36 under the constraint of satisfying initial 4.39 and boundary 4.41 conditions results in solving an initial boundary value problem (IBVP), which embodies the attributes discussed previously in this section. Referring to [29], an IBVP is generally ill-posed since it might not provide any solution, one that is not continuous on the whole initial or boundary data, or one that is nonunique. Considering nonlinear systems of conservation laws, the solution of IBVPs and their analytical treatment becomes very demanding, because general existence theorems cannot be expected. By applying boundary entropy considerations some problem specific results have been obtained with reasonable boundary values, see [29] and the references therein.

CHAPTER 5
FINITE DIFFERENCE SCHEMES FOR ONE-DIMENSIONAL SYSTEMS

Algorithms based on numerical approximation are indispensable in many research disciplines facing complex, "real" world problems. Over the last half century, computational physics have grown to a huge and important field of research challenging complex problems by proposing general methods as well as highly tailored algorithms for all kinds of numerical problems. Therefore, an all-embracing overview on numerical methods for solving nonlinear partial differential equations goes beyond the scope of this thesis and the following introduction only presents a fraction of the existing concepts. This research only considers one-dimensional problems with x denoting the spatial coordinate. Thus, the explanations and derivations in this chapter are also limited to the one-dimensional case.

As mentioned, there exist a wide variety of different numerical methods for approximating solutions to nonlinear partial differential equations. The most common are finite-difference methods, finite-volume methods, finite-element methods, and spectral methods. This classification is based on their representation of approximate solutions. All results presented in this thesis were gathered by utilizing finite-difference methods [34],[30],[26],[35],[36],[37] to approximate the governing problem. For this reason, the subsequent sections solely focus on this approach, while interested readers can find more information about other methods in [38], [31], [39], and the references therein.

First of all, this chapter presents a brief introduction to some general concepts of finite-difference methods and the distinction between upwind and central schemes. In the second part, the numerical scheme - a third-order, semi-discrete Kurganov-Levy scheme [35] - based on a Kurganov-Tadmor scheme [36] used in this research is

described.

5.1 General Concepts

The following sections are especially related to nonlinear, hyperbolic partial differential equations and their numerical solution. The fundamental notions of **consistency**, **convergence**, and **stability** are supposed to be known and will be used without definition (see [34] for corresponding definitions).

First of all, consider the Cauchy problem under the assumption of hyperbolicity

$$\frac{\partial \boldsymbol{u}}{\partial t} + \frac{\partial}{\partial x}\boldsymbol{f}(\boldsymbol{u}) = \boldsymbol{0}, \quad \boldsymbol{u} \,\epsilon\, \mathbb{R}^K, \quad x \,\epsilon\, \mathbb{R}, \quad t > 0 \tag{5.1}$$

$$with \quad \boldsymbol{u}(x,0) = \boldsymbol{u}_0(x). \tag{5.2}$$

Introducing a spatial Δx and temporal Δt scale allows to approximate $\boldsymbol{u}(x_j, t^n)$ at the point ($x_j \coloneqq j\Delta x$, $t^n \coloneqq n\Delta t$) with $\bar{\boldsymbol{u}}_j^n$ as follows

$$\bar{\boldsymbol{u}}_j^{n+1} = \bar{\boldsymbol{u}}_j^n - \lambda \left(\bar{\boldsymbol{f}}_{j+\frac{1}{2}}^n - \bar{\boldsymbol{f}}_{j-\frac{1}{2}}^n \right), \quad j \,\epsilon\, \mathbb{Z}, \quad n \,\geq\, 0 \tag{5.3}$$

with given initial conditions $(\boldsymbol{u}_j^0)_{j\epsilon\mathbb{Z}}$ and $\lambda = \frac{\Delta t}{\Delta x}$ [29]. In general, the continuous function $\bar{\boldsymbol{f}}_{j+\frac{1}{2}}^n$ is specified by

$$\bar{\boldsymbol{f}}_{j+\frac{1}{2}}^n = \bar{\boldsymbol{f}}(\bar{\boldsymbol{u}}_{j-k+1}^n, \ldots, \bar{\boldsymbol{u}}_{j+k}^n) \tag{5.4}$$

where $\bar{\boldsymbol{f}} : \mathbb{R}^{K\times 2k} \to \mathbb{R}^K$ and is denoted the **numerical flux**. According to [29] and [30] the scheme is called to be **consistent** with equation 5.1 if $\bar{\boldsymbol{f}}$ satisfies

$$\bar{\boldsymbol{f}}(\boldsymbol{u}, \ldots, \boldsymbol{u}) = \boldsymbol{f}(\boldsymbol{u}), \quad \forall\, \boldsymbol{u} \,\epsilon\, \mathbb{R}^K. \tag{5.5}$$

In the general case, equation 5.4 represents a $(2K+1)$-point scheme, which reduces to a 3-point scheme for $K = 1$.

A difference scheme with a numerical flux $\bar{\boldsymbol{f}}$ that can be transformed into the form of 5.3 is denoted as **conservative**, and 5.3 is the **conservation form**. In nonlinear partial differential equations spontaneous large gradient phenomena, such as shock development can occur even for sufficient smooth initial data. Thus, it is important to develop so called "shock capturing" methods based on the following fundamental theorem [29],[32],[30].

Lax-Wendroff Theorem. *If $\bar{\boldsymbol{u}}_j^n$ is a discrete solution based on a consistent, conservative difference approximation to a given conservation law initial-value problem (5.1),(5.2) and if $\bar{\boldsymbol{u}}_j^n \to \boldsymbol{u}$ in $L_{1,loc}$ (space of locally Lebesgue integrable functions) as $\Delta x,\ \Delta t \to 0$, then $\boldsymbol{u} = \boldsymbol{u}(x,t)$ is a weak solution to the initial-value problem.*

The **Courant-Friedrichs-Levy condition** (CFL condition) [26], [30],[34] is an important condition for the approximation of (linear) hyperbolic systems, since it states a necessary condition for the convergence of the used scheme. As we saw in chapter 4 for hyperbolic systems, disturbances propagate along the characteristics with finite speed. Therefore, if the analytical domain of dependence is not completely included in the domain of dependence of the numerical scheme, then a change of initial data at the not contained points will influence the true solution of the partial difference equation, but not the numerical solution. As a consequence, the numerical solution can generally not converge to the true solution for all initial data. This results in the following definition [34]

Definition 5.1.1. *A partial differential equation and an associated difference scheme is said to satisfy the Courant-Friedrichs-Lewy (CFL) condition if the analytic domain of dependence, D_a, is contained in the numerical domain of dependence, D_n.*

Figure 5.1 illustrates the domain of dependence of a finite difference method for

a 3-point scheme. The corresponding 3-point scheme is denoted by

$$\bar{\boldsymbol{u}}_j^{n+1} = \bar{\boldsymbol{u}}_j^n - \lambda \left(\bar{\boldsymbol{f}}(\bar{\boldsymbol{u}}_j^n, \bar{\boldsymbol{u}}_{j+1}^n) - \bar{\boldsymbol{f}}(\bar{\boldsymbol{u}}_{j-1}^n, \bar{\boldsymbol{u}}_j^n) \right) \tag{5.6}$$

The discrete, nonlinear CFL condition for a 3-point scheme is specified by

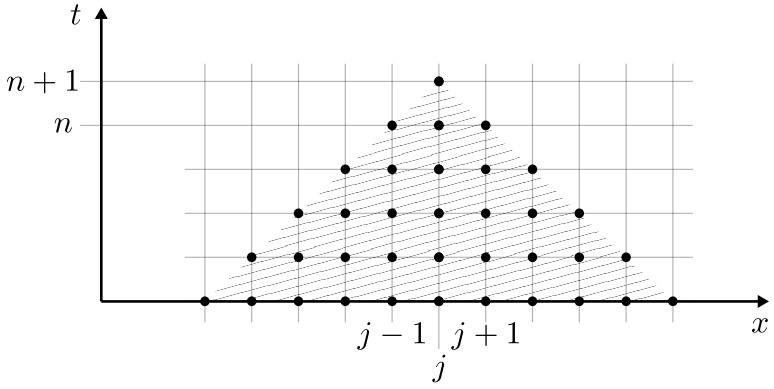

Figure 5.1: Numerical domain of dependence (hatched) for a 3-point scheme (x_j,t_n)

$$\lambda \cdot max(|a_k(\bar{\boldsymbol{u}}_j^n)|) \leq 1, \quad 1 \leq k \leq K \tag{5.7}$$

with $a_k(\bar{\boldsymbol{u}}_j^n)$ denoting the kth eigenvalue $\nu_k(\bar{\boldsymbol{u}}_j^n)$ of the Jacobian matrix $\frac{\partial \bar{\boldsymbol{f}}(\bar{\boldsymbol{u}}_j^n)}{\partial \bar{\boldsymbol{u}}_j^n}$. According to [30] the nonlinear CFL condition 5.7 will be treated as a necessary condition for convergence, even though it is not as apparent as in the linear case. In addition, different particular (nonlinear) schemes might require even more restrictive CFL conditions, which will be noted in the related section.

Even though, the proof of convergence, which is a necessary property for gaining stability is not possible for most methods applied to systems of equations, there exist so called **total variation bounded** (TVB) methods for further investigation of convergence. This section only gives a short introduction to these methods. For a more profound treatment consult [30],[32],[29],[26]. In the scalar case $K = 1$, the discrete **total variation diminishing** (TVD) represents the analogue to the TVB

methods of systems. In this context, total variation diminishing means that the total variation of the (approximate) solution is nonincreasing with time.

Definition 5.1.2. *A difference scheme for scalar conservation laws is said to be total variation diminishing (TVD), if the solution produced by the scheme satisfies*

$$\sum_{j\epsilon\mathbb{Z}} |\bar{u}_{j+1}^{n+1} - \bar{u}_j^{n+1}| \leq \sum_{j\epsilon\mathbb{Z}} |\bar{u}_{j+1}^{n} - \bar{u}_j^{n}|, \quad \forall\, n > 0. \tag{5.8}$$

The solutions of TVD schemes are very desirable, because in addition to providing convergence they exclude spurious oscillations and their accuracy is not restricted to the first order in general. This latter property of not being restricted to first-order accuracy does not hold for 3-point TVD schemes [32]. Thus, obtaining high-order approximations demands at least a 5-point stencil.

The investigation of convergence of systems of hyperbolic equations is not a straightforward extension of the TVD method. Regardless, convergence still necessitates some kind of stability and thus, the notion of **total variation bounded** (TVB) approximations according to [30] is presented in short.

Definition 5.1.3. *A difference scheme (5.1),(5.2) for systems of equations is said to be total variation bounded (TVB), if the solution produced by the scheme satisfies*

$$TV(\bar{\boldsymbol{u}}^n) \leq TV(\bar{\boldsymbol{u}}^{n+1}) \qquad \forall\, n > 0$$

$$\begin{aligned} &with \quad TV((\bar{\boldsymbol{u}}^n)) = \sum_{j\epsilon\mathbb{Z}} ||\bar{\boldsymbol{u}}_{j+1}^{n} - \bar{\boldsymbol{u}}_j^{n}|| \\ &and \quad TV((\bar{\boldsymbol{u}}^{n+1})) = \sum_{j\epsilon\mathbb{Z}} ||\bar{\boldsymbol{u}}_{j+1}^{n+1} - \bar{\boldsymbol{u}}_j^{n+1}|| \end{aligned} \tag{5.9}$$

with $||\cdot||$ *denoting the usual* $\mathbb{R}^K$ *norm.*

The **development of numerical schemes** for the solution approximation of

conservation laws relies on an appropriate approach for the solution inside the defined grid cells. Therefore, the sliding cell average is introduced

$$\bar{\boldsymbol{u}} = \frac{1}{I_x} \int_{I_x} \boldsymbol{u}(\zeta, t) d\zeta \tag{5.10}$$

where $I_x = \left\{\zeta : |\zeta - x| \leq \frac{\Delta x}{2}\right\}$ and the solution is piecewise approximated by the following approach

$$\boldsymbol{u}(x, t^n) = \sum_j \boldsymbol{p}_j(x) \chi_j(x). \tag{5.11}$$

The polynomials $\boldsymbol{p}_j(x)$ are reconstructed from the computed cell-averages $\bar{\boldsymbol{u}}_j^n$ and $\chi_j(x)$ denotes the characteristic function of the cell $I_j := I(x_j)$ with $\chi_j(x) = \mathbf{1}_{[x_j - \frac{\Delta x}{2}, x_j + \frac{\Delta x}{2}]}$ for $\mathbf{1}_{[a,b]} = 1$ in the interval $[a, b]$ and 0 elsewhere. Based on this procedure, different strategies can be pursued leading to the distinction between **upwind** and **central** schemes.

5.2 Upwind vs. Central Schemes

The main characteristic of **upwind schemes** is the evaluation of cell averages 5.10 at the center of the piecewise polynomial approximations. By integration of 5.1 over the rectangle $[x_{j-\frac{1}{2}}, x_{j+\frac{1}{2}}] \times [t_n, t_{n+1}]$ the general formulation of **upwind schemes** is obtained

$$\bar{\boldsymbol{u}}_j^{n+1} = \bar{\boldsymbol{u}}_j^n - \frac{1}{\Delta x} \int_{t^n}^{t^{n+1}} [\boldsymbol{f}(\boldsymbol{u}(x_{j+\frac{1}{2}}, \tau)) - \boldsymbol{f}(\boldsymbol{u}(x_{j-\frac{1}{2}}, \tau))] d\tau. \tag{5.12}$$

Since the cell centers are located at $x = x_j, j \, \epsilon \, \mathbb{Z}$, the fluxes have to be evaluated along the discontinuous cell boundaries, which leads to the challenge of solving local Riemann problems at each cell boundary. Figure 5.2 shows an illustration of an upwind scheme with the local Riemann problems existing at the cell boundaries. In general, Riemann problems can solved by consulting exact or approximate Riemann solvers. Especially solving nonlinear Riemann problems can be very demanding and

is normally done by using approximate Riemann solvers based on Roe linearization. A detailed treatment of Riemann solvers exceeds the scope of this research and can be found in [26], [31],[29], [30].

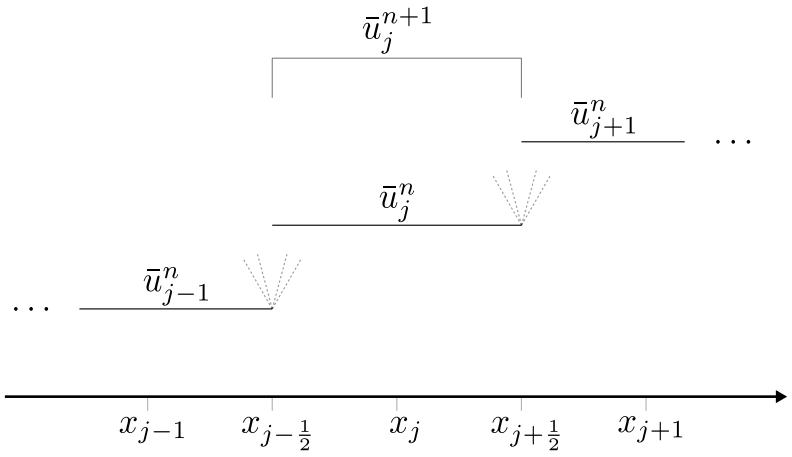

Figure 5.2: Upwind differencing approach for piecewise constant solution with the dotted lines denoting the local Riemann problems

In contrast to upwind schemes, **central schemes** approximate the solution by piecewise evaluation of the staggered averages at the interfacing breakpoints $x = x_{j+1}$. Therefore, integration of 5.1 over the rectangle $[x_j, x_{j+1}] \times [t^n, t^{n+1}]$ leads to

$$\bar{\boldsymbol{u}}_{j+\frac{1}{2}}^{n+1} = \bar{\boldsymbol{u}}_{j+\frac{1}{2}}^{n} - \frac{1}{\Delta x} \int_{t^n}^{t^{n+1}} [\boldsymbol{f}(\boldsymbol{u}(x_{j+\frac{1}{2}}, \tau)) - \boldsymbol{f}(\boldsymbol{u}(x_j, \tau))] d\tau. \tag{5.13}$$

The staggered averaging characterizes central schemes, since the integration over the entire Riemann fan with discontinuities located at $x_{j\pm\frac{1}{2}}$ due to equation 5.11 results in the computation of smooth numerical fluxes at the cell centers $x = x_j$ as depicted in figure 5.3 . This property describes the main advantage of central schemes, because it avoids the necessity of costly (approximate) Riemann solvers. Such Riemann solver free schemes are also called **black box solvers** due to the independence of the scheme to the eigenstructure of investigated system, i.e. no characteristic decomposition is required.

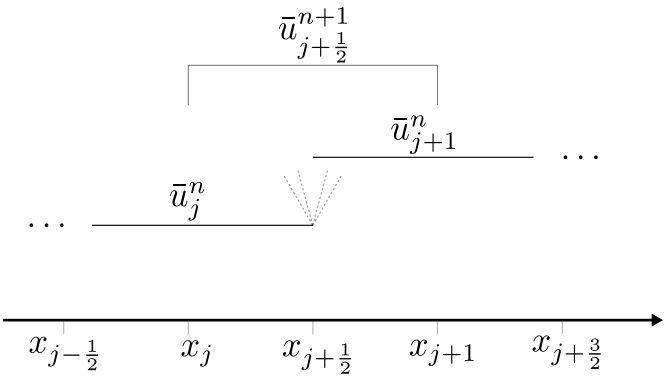

Figure 5.3: Central differencing approach for piecewise constant solution with the dotted lines denoting the local Riemann problem

Contrariwise, one of the disadvantages of central scheme is their high numerical viscosity, and therefore, poor resolution. Particularly, facing problems containing high-gradient phenomena and shock scenarios, requires very small spatial steps and due to the CFL condition (generally yielding $\Delta t << \Delta x$) even smaller time steps. By accumulating the numerical viscosity over the small time steps, the solution smears out and suffers from the bad solution resolution. Higher-order, central scheme proposed by Kurganov and Tadmor [36] achieve to reduce the accumulated numerical viscosity to the order of $O(\Delta x)^{2r-1}$, compared to the order of $O(\frac{(\Delta x)^{2r}}{\Delta t})$ with r denoting an integer.

Another desirable property of central schemes should be mentioned at this point. Besides smearing out steep-gradient solutions, it can occur that numerical schemes introduce non-physical, spurious oscillations to the solution. Remedy can be achieved by the appropriate choice of approximate derivatives, resulting in higher-order approximations, so called non-oscillatory schemes. Fortunately, there exist a collection of recipes for such non-oscillatory reconstructions [32], [36], [37].

5.3 Kurganov-Levy Scheme

This section introduces the numerical scheme used in this research. Based on a collection of high-resolution central schemes proposed by Kurganov and Tadmor [36], Kurganov and Levy developed a third-order, semi-discrete scheme [35], which was utilized for the solution approximation in this thesis.

The difference between semi-discrete schemes, also known as method-of-lines schemes, and the schemes presented above, so called fully-discrete schemes, is that in the semi-discrete case the time evolution is achieved by utilizing an appropriate ODE (ordinary differential equation) solver. A special characteristic of the underlying Kurganov-Tadmor schemes is that they admire a semi-discrete formulation, which is not the general case for central schemes. But especially, since semi-discrete schemes are of high importance for solving "real", practical problems involving multidimentional systems, this characteristic of the Kuganov-Tadmor schemes is an advantageous achievement. Although, this research examines a one-dimensional problem, the semi-discrete scheme is still very effective when combining high-resolution, nonoscillatory spatial discretization with high-order, large stepsize ODE solvers for the time evolution.

All these schemes were developed especially to meet the requirements and cope with the challenges of nonlinear conservation laws and convection-diffusion equations. Besides their main advantage of being Riemann solver free and not requiring an eigenstructure decomposition of the problem under consideration, they provide high resolution even for steep gradient phenomena and shock wave development due to a reduced numerical viscosity. The main idea of the Kurganov-Tadmor and Kurganov-Levy schemes is the use of more precise information about maximum local wave speeds to distinguish between smooth regions and the ones reached by the propagating discontinuities. To maintain a third-order accuracy and being sufficiently nonoscillatory at the same time, Kurganov and Levy utilized a third-order central weighted essen-

tially nonoscillatory (CWENO) reconstruction, which was derived by Levy, Puppo and Russo in [40]. In their paper Kurganov and Levy derive a third-order fully discrete scheme as a first step to, then, reduce it to a corresponding semi-discrete one. In the following only the main ingredients of the resulting semi-discrete scheme are presented. For the full derivation of the schemes, the author refers to [35] and [41].

The final, nonstaggered, semi-discrete formulation of the Kurganov-Levy scheme for the one-dimensional case reads

$$\begin{aligned}\frac{d\bar{\boldsymbol{u}}_j}{dt} =& -\frac{1}{2\Delta x}[\boldsymbol{f}(\boldsymbol{u}^+_{j+\frac{1}{2}}(t)) + \boldsymbol{f}(\boldsymbol{u}^-_{j+\frac{1}{2}}(t)) - \boldsymbol{f}(\boldsymbol{u}^+_{j-\frac{1}{2}}(t)) + \boldsymbol{f}(\boldsymbol{u}^-_{j-\frac{1}{2}}(t))] \\ &+ \frac{a_{j+\frac{1}{2}}(t)}{2\Delta x}[\boldsymbol{u}^+_{j+\frac{1}{2}}(t) - \boldsymbol{u}^-_{j+\frac{1}{2}}(t)] - \frac{a_{j-\frac{1}{2}}(t)}{2\Delta x}[\boldsymbol{u}^+_{j-\frac{1}{2}}(t) - \boldsymbol{u}^-_{j-\frac{1}{2}}(t)]\end{aligned} \tag{5.14}$$

where the local wave speeds $a_{j+\frac{1}{2}}(t)$ are determined through

$$a_{j+\frac{1}{2}}(t) \coloneqq max\left\{\rho\left(\frac{\partial \boldsymbol{f}}{\partial \boldsymbol{u}}(\boldsymbol{u}^-_{j+\frac{1}{2}}(t))\right), \rho\left(\frac{\partial \boldsymbol{f}}{\partial \boldsymbol{u}}(\boldsymbol{u}^+_{j+\frac{1}{2}}(t))\right)\right\}. \tag{5.15}$$

In equation 5.15 $\rho(\boldsymbol{M})$ denotes the spectral radius of a matrix $\boldsymbol{M}$, which is defined as $\rho(\boldsymbol{M}) \coloneqq max_i|\lambda_i(\boldsymbol{M})|$ with the eigenvalues λ_i. The left and right intermediate values of the cell interfaces are named $\boldsymbol{u}^-_{j+\frac{1}{2}}$ and $\boldsymbol{u}^+_{j+\frac{1}{2}}$ and reconstructed in the following way

$$\boldsymbol{u}^-_{j+\frac{1}{2}}(t) = \boldsymbol{A}_j + \frac{\Delta x}{2}\boldsymbol{B}_j + \frac{(\Delta x)^2}{8}\boldsymbol{C}_j, \tag{5.16}$$

$$\boldsymbol{u}^+_{j+\frac{1}{2}}(t) = \boldsymbol{A}_{j+1} - \frac{\Delta x}{2}\boldsymbol{B}_{j+1} + \frac{(\Delta x)^2}{8}\boldsymbol{C}_{j+1} \tag{5.17}$$

with the reconstruction coefficients determined by using the cell averages $\bar{\boldsymbol{u}}^n_{j-1}$,$\bar{\boldsymbol{u}}^n_j$, $\bar{\boldsymbol{u}}^n_{j+1}$, and the weights w_i from the CWENO approach

$$\boldsymbol{A}_j = \bar{\boldsymbol{u}}^n_j - \frac{w_C}{12}(\bar{\boldsymbol{u}}^n_{j+1} - 2\bar{\boldsymbol{u}}^n_j + \bar{\boldsymbol{u}}^n_{j-1}), \tag{5.18}$$

$$\boldsymbol{B}_j = \frac{1}{\Delta x}\left[w_R(\bar{\boldsymbol{u}}^n_{j+1} - \bar{\boldsymbol{u}}^n_j) + w_C\frac{\bar{\boldsymbol{u}}^n_{j+1} - \bar{\boldsymbol{u}}^n_{j-1}}{2} + w_L(\bar{\boldsymbol{u}}^n_j - \bar{\boldsymbol{u}}^n_{j-1})\right], \tag{5.19}$$

$$\boldsymbol{C}_j = 2w_C\frac{\bar{\boldsymbol{u}}^n_{j-1} - 2\bar{\boldsymbol{u}}^n_j + \bar{\boldsymbol{u}}^n_{j+1}}{(\Delta x)^2}. \tag{5.20}$$

Finally, the time evolution is carried out by a third-order strong stability-preserving (SSP) Runge-Kutta solver proposed by Gottlieb, Shu, and Tadmor in [42].

The intermediate values $\boldsymbol{u}^-_{j-\frac{1}{2}}(t)$, $\boldsymbol{u}^+_{j-\frac{1}{2}}(t)$ and therefore, the local wave speeds $a_{j-\frac{1}{2}}(t)$ at $x = x_{j-\frac{1}{2}}$ can be calculated in the same manner as shown above for $x = x_{j+\frac{1}{2}}$.

CHAPTER 6
SIMULATION SETUP

This chapter depicts the steps from the governing equation 3.11 to information extracted from the numerical solution. First, the general solution procedure used in this thesis is illustrated. Second, the implementation of equation 3.11 in the numerical scheme by transcribing equation 3.11 into conservation form is presented. As a third step, appropriate initial conditions are defined before the evaluation of the results is discussed in a signal processing section. Finally, numerical parameters, e.g. CFL condition and spatial discretization are stated and some results are shown for their validation.

6.1 Solution Procedure

The solution procedure is based on the transformation of equation 3.11 into conservation form. The conservation form can be, then directly implemented into the numerical algorithm together with appropriate initial and boundary conditions. A schematic of this procedure for the implementation is shown in figure 6.1.

It is important to mention that the one-dimensional wave equation is a second-order equation and therefore waves are propagating in both - positive and negative - spatial directions x. As we will see in section 6.3, that we apply nonzero, initial conditions to our problem, this fact is valid. The initial conditions will be applied in the center of our spatial domain and two equivalent waves will travel in different spatial directions.

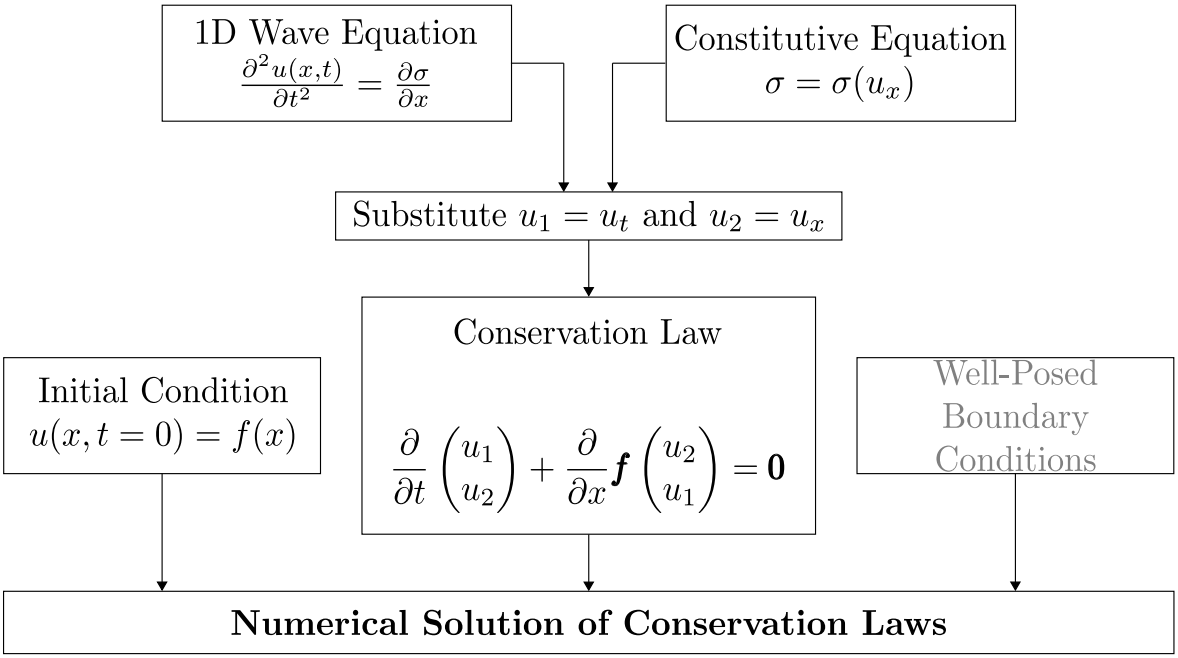

Figure 6.1: Schematic of the solution procedure of the one-dimensional wave equation with the nonlinear stress-strain relationship of the combined model adapted from [43]

6.2 Conservation Form

Recall equation 3.11

$$\frac{\partial^2 u}{\partial t^2} - c_{L,c}^2 \frac{\partial^2 u}{\partial x^2} = -c_{L,c}^2(\gamma_c f_c(u) - \gamma_t f_t(u)) - c_{L,c}^2 \gamma_a (f_{q,c}(u) - f_{q,t}(u)), \tag{6.1}$$

with the corresponding auxiliary functions 3.12

$$\begin{aligned} f_c(u) &= H[\frac{\partial u}{\partial x} - \varepsilon_1]\frac{\partial^2 u}{\partial x^2}, \qquad f_t(u) = H[\frac{\partial u}{\partial x} - \varepsilon_2]\frac{\partial^2 u}{\partial x^2}, \\ f_{q,c}(u) &= H[\frac{\partial u}{\partial x} - \varepsilon_1]\frac{\partial u}{\partial x}\frac{\partial^2 u}{\partial x^2}, \qquad f_{q,t}(u) = H[\frac{\partial u}{\partial x} - \varepsilon_2]\frac{\partial u}{\partial x}\frac{\partial^2 u}{\partial x^2}. \end{aligned} \tag{6.2}$$

The utilized Kurganov-Levy scheme requires the formulation of the governing equation in conservation form. Thus, the second-order wave equation 6.1, where our scalar u denotes the particle displacement, has to be reduced to a system of two first-order

equations by substituting $\frac{\partial u}{\partial t} = u_1$ and $\frac{\partial u}{\partial x} = u_2$. Applying the auxiliary functions 6.2 leads to the following system of equations

$$\frac{\partial}{\partial t}\begin{pmatrix} u_1 \\ u_2 \end{pmatrix} + \frac{\partial}{\partial x}\boldsymbol{f}\begin{pmatrix} u_2 \\ u_1 \end{pmatrix} = \mathbf{0}, \tag{6.3}$$

where

$$\boldsymbol{f}(\boldsymbol{u}) = \tag{6.4}$$

$$\begin{pmatrix} (-c_{L,c}^2 u_2)(1 - \gamma_c H(u_2 - \varepsilon_1) + \gamma_t H(u_2 - \varepsilon_2) - \gamma_a H(u_2 - \varepsilon_1)u_2 + \gamma_a H(u_2 - \varepsilon_2)u_2) \\ -u_1 \end{pmatrix}$$

is called the flux function. The interdependent variables u_1 and u_2 denote the particle velocity and the strain, respectively.

6.3 Initial Conditions

As mentioned in section 4.3.2, the solution of partial differential equation requires the specification of initial and boundary conditions. In this research, the investigated wave never reaches the boundaries of the spatial domain and therefore defining boundary conditions becomes unnecessary at this point.

Since the obtained conservation form 6.3 with the flux function 6.4 is a system of two partial differential equations, it demands the specification of two initial conditions, one for each variable u_i. The initial particle velocity $u_1(x, t = 0) = u_t(x, t = 0)$ is set to zero, since the considered specimen is assumed to be in a state of rest at time $t = 0$

$$u_1(x, 0) = 0. \tag{6.5}$$

The initial strain $u_2(x, t = 0) = u_x(x, t = 0)$ is defined in a way that it represents the

excitation of the specimen with an ultrasonic signal. The following burst signal

$$u_2(x,0) = q(x)A_0 cos(k_0 x) \tag{6.6}$$

where the coefficient $q(x)$ stems from a Tukey windowing function and is defined as

$$q(x) = \begin{cases} \frac{1}{2}\left\{1 + cos\left(\frac{2\pi}{r}\left[x - \frac{r}{2}\right]\right)\right\}, & 0 \leq x < \frac{r}{2} \\ 1, & \frac{r}{2} \leq x < 1 - \frac{r}{2} \\ \frac{1}{2}\left\{1 + cos\left(\frac{2\pi}{r}\left[x - 1 + \frac{r}{2}\right]\right)\right\}, & 1 - \frac{r}{2} \leq x \leq 1. \end{cases} \tag{6.7}$$

The parameter r denotes the ratio between the tapered part of the cosine to the total length of the signal and is set to $r = 0.5$ for all presented examples.

As a next step the excitation amplitude A_0 and wave number k_0 have to be specified. Since the initial signal should simulate an ultrasonic excitation, these values were chosen according to typical values used for such experiments. The initial strain amplitude is set to $A_0 = 2.63e-6$ for most of the experiments. The results discussion will show that some examples required a change of the input amplitude, which will be mentioned accordingly. The specification of the wave number k_0 is derived from a common fundamental temporal frequency $f_0 = 5\text{MHz}$, which is used for lab experiments with nonlinear ultrasound by

$$k_0 = \frac{2\pi f_0}{c_{L,c}} \approx 5260.54\frac{1}{m} \quad with \quad c_{L,c} = 5972\frac{m}{s}. \tag{6.8}$$

In the next section about signal processing we will see that we use the (fundamental) spatial frequency f_S more often in this research than the (fundamental) temporal frequency f. Note that both frequencies are related by the following equation

$$f_S = \frac{f}{c_{L,c}} \quad with \quad c_{L,c} = 5792\frac{m}{s} \tag{6.9}$$

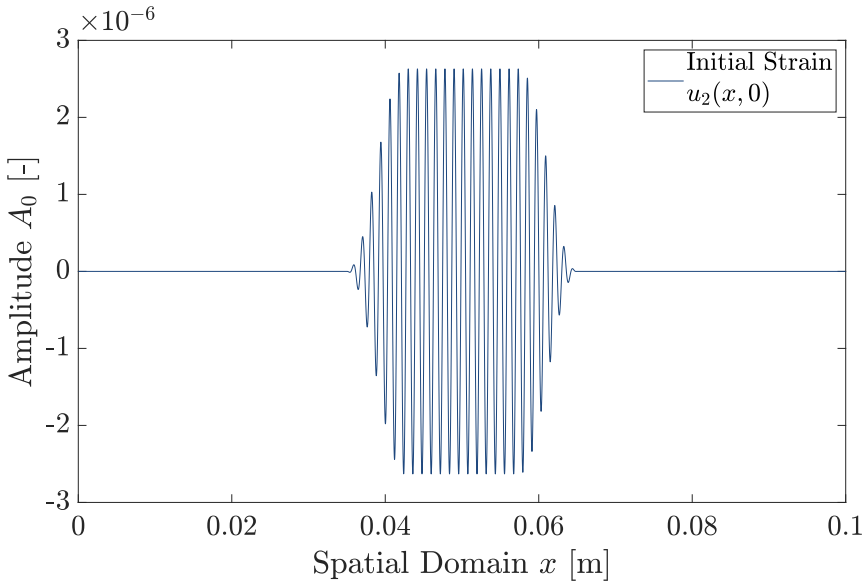

Figure 6.2: Initial strain input $u_2(x, 0)$

and therefore, a temporal frequency of $f_0 = 5\text{MHz}$ corresponds to a spatial frequency of $f_{S0} \approx 837.24\frac{1}{m}$. Figure 6.2 depicts the resulting initial strain signal. The cosine tapering at the edges of the signal is used to fade the nonzero part of the signal to avoid numerical artifacts from jump-like changes in the initial signal. At some time $t > 0$ the initial wave is splitted into two waves each with half the initial amplitude traveling in different spatial directions.

6.4 Signal Processing

The numerical algorithm outputs the propagated (left- and right-going) particle velocity u_1 and strain waves u_2 over the whole spatial domain after a desired time of propagation $t > 0$. Since this research is especially interested in the generation of second harmonic amplitudes, these outputs have to be analyzed accordingly.

The analysis is performed by applying a Fast Fourier Transformation (FFT), a

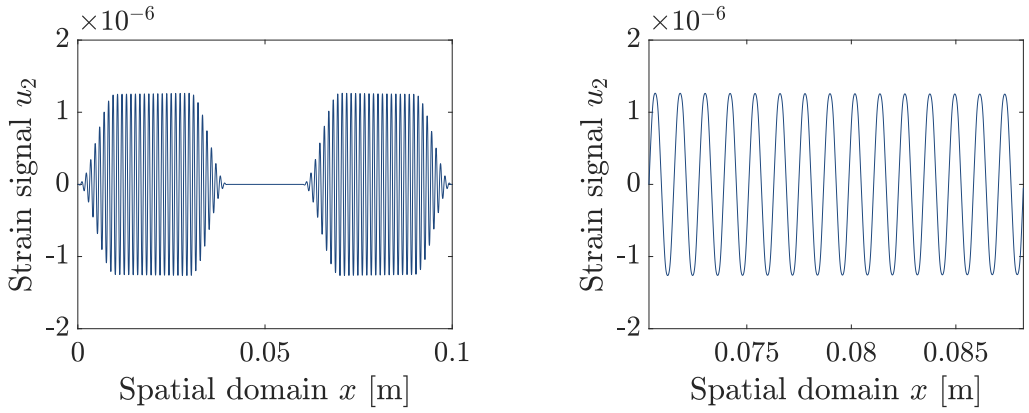

(a) Whole numerical result (b) Tailored numerical result for FFT

Figure 6.3: Tailoring of the numerical results for the FFT analysis

default function of MATLAB to the strain signal u_2. The FFT is implemented by

$$X(k) = \sum_{j=1}^{N} x(j)\omega_N^{(j-1)(k-1)}, \tag{6.10}$$

where $\omega_N = e^{-\frac{i2\pi}{N}}$ and $N = length(x)$ denotes the length of the signal. The FFT transforms the space-domain signal into the (spatial) frequency domain. The spatial and the temporal frequency domain are related by equation 6.9. Plotting the resulting FFT signal allows the analysis of occurring higher harmonics and their corresponding amplitudes, which is what this research aims for.

To receive appropriate results from the FFT analysis the cosine-tapered signal has to be tailored according to the spatial discretization, which determines the sampling frequency of the FFT and the fundamental excitation frequency f_0. Another reason is that we want to determine the exact amplitudes of the higher - especially the second - harmonics and therefore, the tapered regions of the initial signal distort the FFT results. As a consequence, before applying the FFT analysis, a homogeneous, "full-amplitude" part is cut out of the spatial domain. Figure 6.3 shows such a tailored signal.

6.5 Numerical Parameters

This section introduces the consulted parameters for the numerical approximation. Particularly, the propagation distance x_p, the spatial discretization Δx and the CFL condition are discussed and the latter ones validated with some numerical results in the following.

6.5.1 Propagation Distance x_p

The propagation distance x_p is set to a constant value of $x_p = 0.03$m for all simulations. The reason for setting x_p constant over all simulations is due to the fact that the acoustic nonlinearity parameter β is dependent of the propagation distance x_p (denoted by x) according to equation 2.15. To maintain comparability of multiple simulations with different material parameters the propagation distance x_p has to stay constant.

6.5.2 Spatial Discretization Δx

The considered one-dimensional spatial domain is denoted by x and represents a length of $0.1m$. This continuous spatial domain is discretized with a one-dimensional grid consisting of $N = 10000$ points leading to a spatial step of $\Delta x = 10^{-5}$m. For numerical approximations the spatial step size is a crucial parameter to choose, especially when dealing with steep gradient phenomena and/or high-frequency waves. This research involves high-frequency waves $f_0 = 5MHz$ as well as steep gradient phenomena as we will see in the result section. Therefore, one has always to find a compromise between high enough resolution of the numerical scheme and reasonable computation time.

The spatial step size was chosen according to the investigations of Küchler et al. [44] and the references therein. Küchler et al. proved the convergence of a related

semi-discrete Kuganov-Tadmor scheme to the analytical solution of a linear lamb wave problem with the same fundamental frequency $f_0 = 5MHz$. By refinement of the spatial step, Küchler et al. showed that the numerical error vanishes as well as artificially introduced odd harmonics in the FFT signal, which result from a bad spatial resolution. They conclude that a spatial resolution of 60 gridpoints per wavelength is high enough, while retaining an affordable computational effort.

Since this research only deals with one spatial dimension, compared to Küchler et al. who examined two-dimensional problems the computational effort is smaller in general. Reversely this means, for a one-dimensional problem the spatial resolution can be increased while retaining an affordable computational time. Thus, a two-times finer spatial discretization than Küchler et al. suggested of 120 gridpoints per wavelength was used for this thesis. A wavelength of $\lambda_0 = \frac{2\pi}{k_0} \approx 1.2 \cdot 10^{-3}m$ and 120 gridpoints per wavelength lead to a spatial step size of $\Delta x = 10^{-5}$m.

Figure 6.4 shows the results of the Kurganov-Levy scheme to the linear wave equation with a spatial discretization of $\Delta x = 10^{-6}$m (red dotted line) and $\Delta x = 10^{-5}$m (blue solid line) plotted in one graph. It seems that both discretizations represent the general shape of the solution to the linear wave equation properly. Nevertheless, the higher discretization with 1200 per wavelength presents slightly higher amplitudes due to the fact that it can obviously better approximate the narrow peaks of the wave. If we perform a FFT analysis of both signals according to section 6.4, we receive the graphs shown in figure 6.5. Even though the results in figure 6.4 appear to be almost the same, the FFT shows that the lower spatial discretization clearly introduces higher odd $(3f_0, 5f_0, 7f_0, \dots)$ harmonics. This phenomenon was also detected by Küchler et al. Since we know from chapter 2.1 that the linear case does not generate higher harmonics, this artifact has to stem from the lower discretization.

Despite this fact, a spatial discretization of $\Delta x = 10^{-5}$ relating to 120 gridpoints

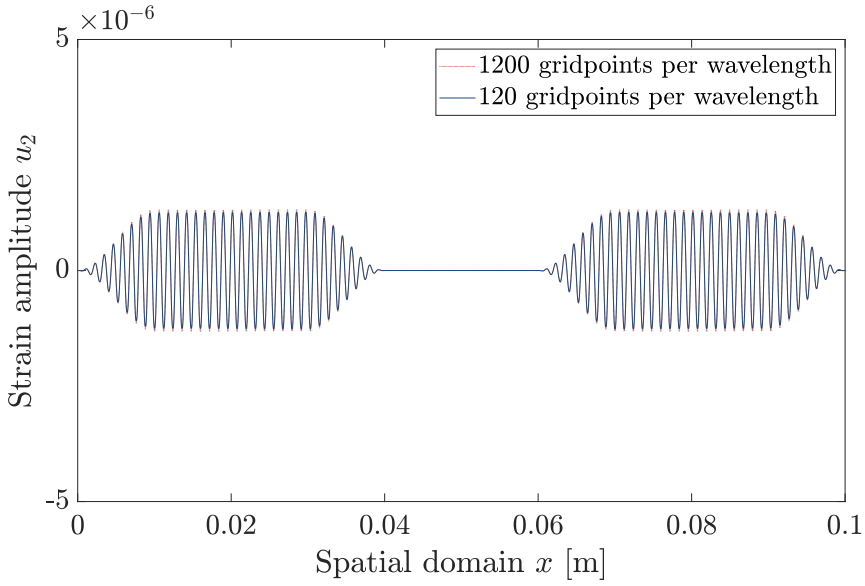

Figure 6.4: Numerical solution for the linear wave equation of the Kurganov-Levy scheme with a spatial discretization of $\Delta x = 10^{-6}$m (red dotted line) and $\Delta x = 10^{-5}$m (blue solid line)

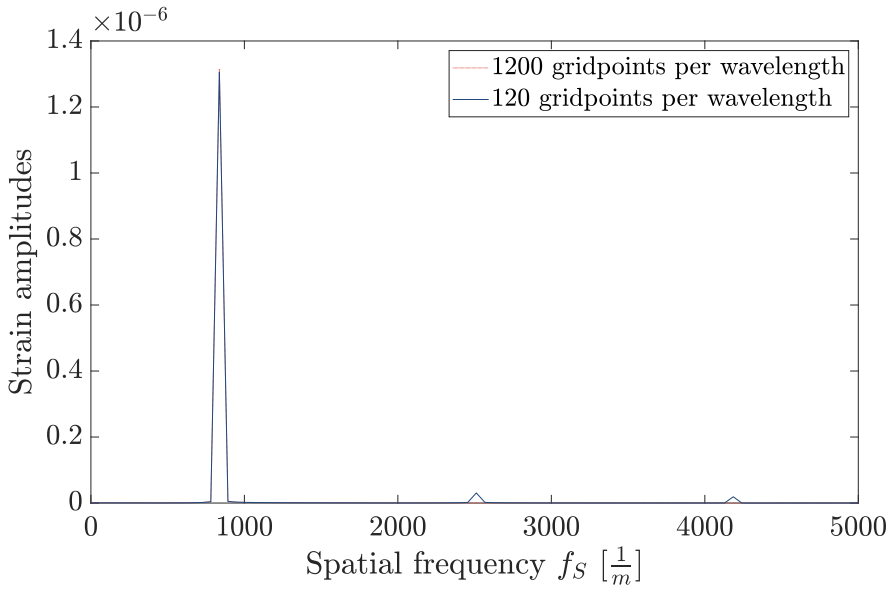

Figure 6.5: FFT result of the numerical solution for the linear wave equation with a spatial discretization of $\Delta x = 10^{-6}$m (red dotted line) and $\Delta x = 10^{-5}$m (blue solid line)

is assumed to be high enough for several reasons. First, this research only investigates the first and second harmonic amplitudes for the most part, such that the artificially generated higher odd harmonics do not interfere with this examination. Second, the "loss" of amplitude in the FFT due to the lower discretization is about 0.68%, which is assumed to be neglectable. And third, the computation time choosing the higher discretization would be increased by a factor of approximately 200 leading to a computational time of multiple days for a single simulation, which is not affordable for a parameter study like the one in this research.

6.5.3 CFL Condition

Chapter 5 displayed the importance of the Courant-Friedrichs-Levy (CFL) condition, which ensures that the analytic domain of dependence is completely contained in the numerical domain of dependence for the convergence of a numerical scheme. It was also mentioned that for nonlinear systems of equations, there does not necessarily exist CFL condition that reassures the convergence of the scheme to the analytical solution.

However, Kurganov and Levy do not provide such a CFL condition for their scheme in the corresponding publication [35]. According to Küchler et al. [44] a second-order, semi-discrete scheme related to the utilized Kurganov-Levy scheme has to fulfill the following algorithm-dependent CFL condition for converging to the analytical solution

$$\frac{\Delta t}{\Delta x}\left(a_{j+\frac{1}{2}}(t)\right) \leq \frac{1}{2} \quad \forall\, j \tag{6.11}$$

where $a_{j+\frac{1}{2}}$ denote the local wave speeds as defined in equation 5.15. As a consequence the time step was chosen to be $\Delta t = 6.55 \cdot 10{-}10\text{s}$. Together with a spectral radius of $\rho(\boldsymbol{M}) \approx 6104$ determined as described in chapter 5 and a spatial discretization $\Delta x = 10^{-5}$, this time step holds even for a little more restrictive CFL condition of 0.4 than 6.11 requires.

Especially, since Kurganov and Levy do not provide a general CFL condition, we need to validate our choice of the CFL condition and thus, the choice of our time step Δt. This is done by comparing results computed with a time step of $\Delta t = 6.55 \cdot 10{-}10\text{s}$ relating to a CFL condition of 0.4 with results computed with $\Delta t = 1.64 \cdot 10^{-11}\text{s}$, which relates to a very restrictive CFL condition of 0.01. Figure 6.6 shows the numerical results and the corresponding FFT analyses for the linear wave equation (a),(b),(e) and the nonlinear equation 6.1 (c),(d),(f). The strain signal and the FFT analyses already suggest that the numerical results are very similar for both CFL conditions. This hypothesis is confirmed when taking into account the difference plots (e),(f) of the FFT-signals for the linear and nonlinear equation, since the FFT-signals for the second harmonic amplitude only differ by the order of 10^{-11}, which is neglectable.

This concludes that a CFL condition of 0.4 with a corresponding time step $\Delta t = 6.55 \cdot 10{-}10\text{s}$ ensures convergence of the scheme for the consulted parameters. A smaller time step enforced through a more restrictive CFL condition does neither improve nor alter the numerical results.

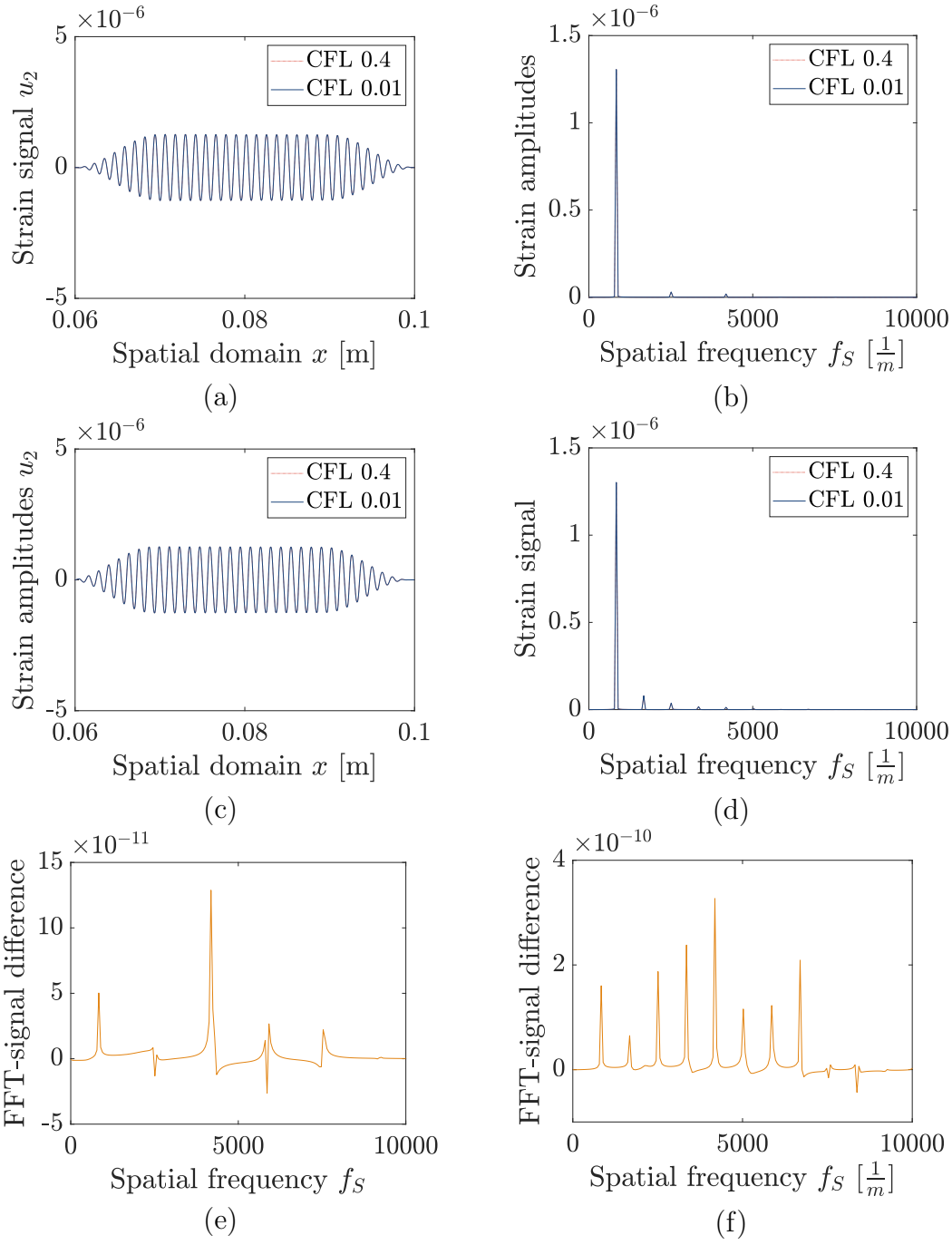

Figure 6.6: Numerical results for the linear (a),(b),(e) and nonlinear (c),(d),(f) wave equation with CFL conditions of 0.4 (dotted red line) and 0.01 (solid blue line)

CHAPTER 7

RESULTS

This chapter presents the numerical results, obtained with a third-order, semi-discrete Kurganov-Levy scheme, for a monochromatic wave propagating in a material with distributed microcracks, whose constitutive relationship was derived by a combined micromechanical modeling approach.

The objective of this research is to determine a relationship between the acoustic nonlinearity parameter β and crack parameters of the material. If we recall equation 3.11 with 3.12 and figure 7.1, which illustrates the overall nonlinear stress-strain

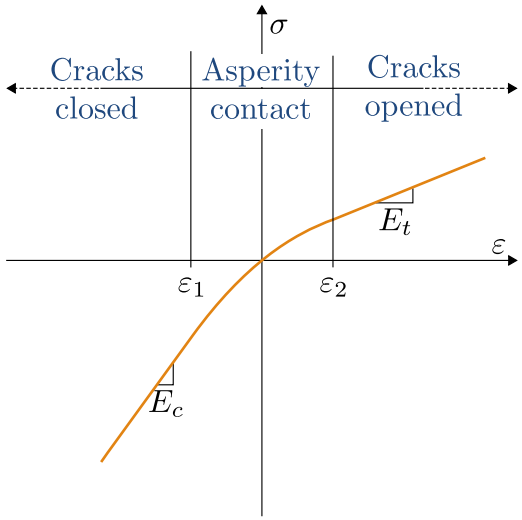

Figure 7.1: Schematic of the overall nonlinear stess-strain relationship of the combined model adapted from [18]

relationship of the cracked material, one can easily imagine that the material behaves not only differently for various crack parameters, but also depends on the excitation amplitude A_0. As a consequence the following chapter is divided into three sections acting like a decomposition of the problem under consideration. Since it is difficult to validate the overall numerical solution for the more complex combined model, this

incremental approach has been chosen.

The first two sections focus on the quadratic part of the stress-strain relationship, where we deal with small enough excitation amplitudes that stay within the transition values ε_1 and ε_2. Such small amplitudes lie in the range of excitation amplitudes used for second harmonic generation measurements and are therefore of great interest for nondestructive evaluation.

The third section applies high amplitudes to the combined model in order to examine the materials' behavior around and above the transition values ε_1 and ε_2 to take the whole model into account. Such strong excitation simulations are important to estimate the materials' state after it was exposed to high impacts, e.g. due to misuse or (unexpected) high loads.

As seen in chapter 3, the combined model requires the specification of material parameters in order to represent the material under consideration. Since this research is deducted on the example of NFAs, we will use the material parameters from Hoffmann et al. as a basis to start from. Recalling table 3.1, it illustrates all relevant material parameters required for the combined model.

Table 7.1: Numerical material parameters for NFAs [18]

Symbol	**Value**	**Explanation**
E	190 GPa	Young's modulus of the uncracked material
ν	0.25	Poisson's ratio of the uncracked material
R	$0.5 \cdot 10^{-3}$ m	crack radius
N_0	$3 \cdot 10^{8}$ m	number of cracks per m^3
h_S	10^{-8} m	$\sqrt{2}$times effective height of asperities
d_0	$3 \cdot 10^{-8}$ m	initial distance between crack faces
$c_{L,c}$	5972 m/s	longitudinal wave velocity

Note that the thickness of the specimen, which relates to the propagation distance of the wave and the circular frequency is not contained in the following table anymore,

since they have been chosen differently for this research (see section 6.5). The following sections demand the change of specific material parameters in order to investigate the materials' behavior. These changes will be denoted in the corresponding sections, while unstated parameters remain constant according to table 7.1.

7.1 Quadratic Nonlinearity - Relation between A_1, A_2, and β_{RSC}

After section 6.5 proved that the numerical scheme leads to good results for the linear wave equation, we want to confirm that the scheme also works for the nonlinear case. Besides that, it should be verified that the combined model results in the expected proportional relationship between $\frac{A_2}{A_1^2}$ and β_{RSC}. Therefore, a series of simulations is run with the same excitation amplitude A_0 and different acoustic nonlinearity parameter values. Since we only consider the quadratic part of the stress-strain relationship in this section, an excitation amplitude of $A_0 = 2.63 \cdot 10^{-6}$ is applied. This value relates to a common displacement amplitude of 0.5 nm in second harmonic generation measurements.

The overall goal of the combined model as well as the numerical scheme is to represent reality as best as possible. Thus, we need to ensure that we only implement parameters according to all conditions of the combined model. If we want to change the acoustic nonlinearity parameter β_{RSC} in the quadratic part of the model, we have to change some material parameter according to equation 3.4

$$G_2 = \frac{N_0 R^4 h_s (16\nu^2 - 16)^2}{9 d_0^2 \pi \frac{N_0 R^3 h_s (16\nu^2 - 16)}{3 d_0 (h_s/d_0 + 1) - 1})^2 (h_s/d_0 + 1)^3} \equiv \beta_{RSC}. \tag{7.1}$$

This equation offers five parameters to us, which might be subject to change. But since we want to investigate the influence of the macroscopic crack parameters N_0 and R later on, we leave them untouched in this section. The Poisson ratio ν remains constant as well, because its influence on β_{RSC} is comparatively low. For this reason,

only two microscopic values h_S, the $\sqrt{2}$times effective height of asperities and d_0, the initial distance between crack faces are left. According to Kim et al. [45], the $\sqrt{2}$times effective height of asperities $h_S = 1 \cdot 10^{-8}$ m chosen by Hoffmann et al. is relatively low, which relates to ultra smooth crack faces. Therefore, the parameter h_S can be varied over a wide range representing crack faces from ultra smooth to very rough and it strongly influences β_{RSC} within this range. As a consequence, the parameter d_0 stays constant for most of the simulations and is only changed for very high β_{RSC}-values. Table 7.2 shows all combinations of the parameters h_S and d_0 together with the resulting acoustic nonlinearity parameters β_{RSC} used for the simulations. Furthermore, table 7.2 indicates that we do not cross the transitions ε_1

Table 7.2: Parameter combinations of h_S and d_0 with the resulting β_{RSC}-values and transitions ε_1,ε_2

h_S	d_0	β_{RSC}	ε_1	ε_2
$6.00 \cdot 10^{-7}$	$3.0 \cdot 10^{-8}$	7.73	$-2.31 \cdot 10^{-2}$	$9.72 \cdot 10^{-4}$
$4.50 \cdot 10^{-7}$	$3.0 \cdot 10^{-8}$	13.17	$-1.33 \cdot 10^{-2}$	$7.49 \cdot 10^{-4}$
$3.25 \cdot 10^{-7}$	$3.0 \cdot 10^{-8}$	23.69	$-7.20 \cdot 10^{-3}$	$5.63 \cdot 10^{-4}$
$2.00 \cdot 10^{-7}$	$3.0 \cdot 10^{-8}$	54.40	$-3.00 \cdot 10^{-3}$	$3.79 \cdot 10^{-4}$
$1.50 \cdot 10^{-7}$	$3.0 \cdot 10^{-8}$	86.12	$-1.80 \cdot 10^{-3}$	$3.06 \cdot 10^{-4}$
$1.30 \cdot 10^{-7}$	$3.0 \cdot 10^{-8}$	106.99	$-1.40 \cdot 10^{-3}$	$2.77 \cdot 10^{-4}$
$1.15 \cdot 10^{-7}$	$3.0 \cdot 10^{-8}$	127.96	$-1.20 \cdot 10^{-3}$	$2.55 \cdot 10^{-4}$
$1.00 \cdot 10^{-7}$	$3.0 \cdot 10^{-8}$	155.62	$-9.27 \cdot 10^{-4}$	$2.34 \cdot 10^{-4}$
$8.00 \cdot 10^{-8}$	$3.0 \cdot 10^{-8}$	208.35	$-6.55 \cdot 10^{-4}$	$2.07 \cdot 10^{-4}$
$7.00 \cdot 10^{-8}$	$3.0 \cdot 10^{-8}$	244.85	$-5.36 \cdot 10^{-4}$	$1.93 \cdot 10^{-4}$
$3.20 \cdot 10^{-8}$	$3.0 \cdot 10^{-8}$	499.64	$-1.94 \cdot 10^{-4}$	$1.53 \cdot 10^{-4}$
$1.00 \cdot 10^{-8}$	$3.0 \cdot 10^{-8}$	638.18	$-7.35 \cdot 10^{-5}$	$1.86 \cdot 10^{-4}$
$1.00 \cdot 10^{-8}$	$2.5 \cdot 10^{-8}$	783.79	$-6.83 \cdot 10^{-5}$	$1.44 \cdot 10^{-4}$
$1.00 \cdot 10^{-8}$	$2.0 \cdot 10^{-8}$	979.04	$-6.38 \cdot 10^{-5}$	$1.08 \cdot 10^{-4}$

and ε_2 for the chosen excitation amplitude of $A_0 = 2.63 \cdot 10^{-6}$ and therefore, only

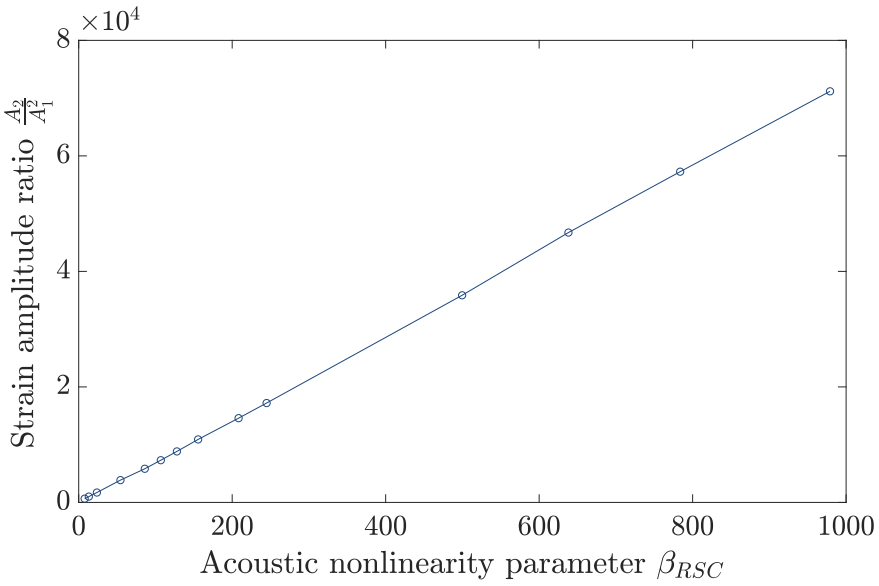

Figure 7.2: Ratio of the first and second harmonic $\frac{A_2}{A_1^2}$ over the acoustic nonlinearity parameter β_{RSC}

the quadratic part of the combined model is considered. This fact has to be checked whenever a single material parameter is changed, since we know from equation 3.6 and the underlying equations 3.5 and 3.4 that the transitions ε_1 and ε_2 change depending on the material parameters.

Figure 7.2 shows the resulting relation between $\frac{A_2}{A_1^2}$ and the acoustic nonlinearity parameter β_{RSC} of the quadratic part of the combined model. The first and second harmonic amplitudes A_1 and A_2 are evaluated as described in 6.4 by processing an FFT analysis. Figure 7.2 clearly illustrates that the acoustic nonlinearity parameter β_{RSC} of the quadratic part is linearly related to the ratio $\frac{A_2}{A_1^2}$ of the first and second harmonic amplitudes. This dependency was expected, because as mentioned in section 3.3.3 the definition of the acoustic nonlinearity parameter β_{RSC} of the Rough Surface Contact model, which is considered in the quadratic part of the combined model, is proportional to $\frac{A_2}{A_1^2}$ according to the definition in equation 2.15

$$\beta = \frac{8A_2}{A_1^2 x k^2} = \frac{8A_2 c_L^2}{A_1^2 \omega^2 x}. \tag{7.2}$$

Finally, these results confirm that the combined model of Hoffmann et al. [18] together with the applied numerical approximation work properly for small excitation amplitudes that only activate the quadratic part of the model. Hence, it can be used to simulate materials' behavior in nondestructive ultrasonic testing, where such small amplitudes are usually applied. Further, it proves that the numerical scheme provides appropriate solutions for a nonlinear wave equation.

7.2 Quadratic Nonlinearity - Dependency on Crack Parameters

The previous results confirmed that the numerical scheme provides good results for the quadratic part of the combined model. Based on that, this section section examines the dependency of the acoustic nonlinearity parameter β_{RSC} on the crack parameters N_0 (number of crack per cubic meter) and R (crack radius) by evaluating $\frac{A_2}{A_1^2}$.

First, recall the following equation for the acoustic nonlinearity parameter β_{RSC} of the quadratic part of the combined model

$$G_2 = \frac{N_0 R^4 h_s (16\nu^2 - 16)^2}{9 d_0^2 \pi \frac{N_0 R^3 h_s (16\nu^2 - 16)}{3 d_0 (h_s/d_0 + 1) - 1})^2 (h_s/d_0 + 1)^3} \equiv \beta_{RSC}. \tag{7.3}$$

From this equation we can deduce that the crack parameters of interest N_0 and R influence the acoustic nonlinearity parameter β_{RSC} differently. As a consequence, they cannot be summarized and then investigated by variation of the combined parameter crack density c, which relates the number of cracks per cubic meter N_0 and crack radius R by the following equation

$$c = N_0 R^3. \tag{7.4}$$

In contrast, the influence of N_0 and R is examined separately by varying one parameter and keeping the other constant.

Again, we need to ensure that we choose our material parameters in an appropriate

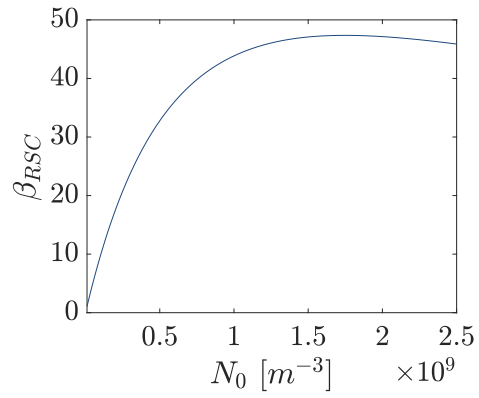

(a) β_{RSC} over number of cracks per cubic meter N_0 $[m^{-3}]$

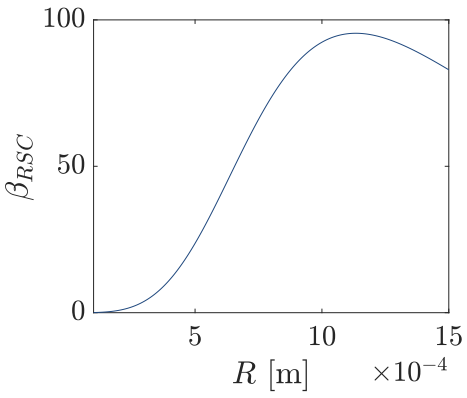

(b) β_{RSC} over crack radius R $[m]$

Figure 7.3: Dependency of the acoustic nonlinearity parameter β_{RSC} on the crack parameters N_0 and R according to the combined model

manner, such that we do not cross the changing transitions ε_1, ε_2 with our excitation amplitude $A_0 = 2.63 \cdot 10^{-6}$ while varying the crack parameters N_0 and R. To provide a meaningful range for varying these parameters, the material parameters are chosen as depicted in table 7.1 except for the $\sqrt{2}$times effective height of asperities, which is changed to $h_S = 3.25 \cdot 10^{-7}$m according to the "smooth-smooth" case of [45]. After setting the material parameters, we know from equation 7.3 how the acoustic nonlinearity parameter β_{RSC} changes over different N_0 and R. Figure 7.3 illustrates this relationship for the number of cracks per cubic meter N_0(a) and the crack radius R(b). By comparing the ratio $\frac{A_2}{A_1^2}$ of the strain amplitudes with these courses 7.3, we can make a statement about how well the numerical scheme solves the governing equations up to the limits of the combined model.

7.2.1 Number of Cracks per cubic meter N_0

As mentioned previously, the $\sqrt{2}$times effective height of asperities h_S was set to a value of $h_S = 3.25 \cdot 10^{-7}$m for the simulations of this whole section. For the investigation of the influence of N_0, the crack radius R is fixed to the value $R = 5 \cdot 10^{-4}$ chosen by Hoffmann et al. for the combined model, while N_0 is varied from $2 \cdot 10^7 m^{-3}$

to $2 \cdot 10^9 m^{-3}$. Table 7.3 shows the exact variation of the relevant parameters. Again,

Table 7.3: Parameter variation of N_0 and the resulting values for the crack density c, β_{RSC} and transitions ε_1,ε_2

N_0	R	c	β_{RSC}	ε_1	ε_2
$4.00 \cdot 10^7$	$5 \cdot 10^{-4}$	$5.00 \cdot 10^{-3}$	4.14	$-5.50 \cdot 10^{-3}$	$4.97 \cdot 10^{-4}$
$8.00 \cdot 10^7$	$5 \cdot 10^{-4}$	$1.00 \cdot 10^{-2}$	7.93	$-5.80 \cdot 10^{-3}$	$5.08 \cdot 10^{-4}$
$1.00 \cdot 10^8$	$5 \cdot 10^{-4}$	$1.25 \cdot 10^{-2}$	9.70	$-5.90 \cdot 10^{-3}$	$5.13 \cdot 10^{-4}$
$3.00 \cdot 10^8$	$5 \cdot 10^{-4}$	$3.75 \cdot 10^{-2}$	23.69	$-7.20 \cdot 10^{-3}$	$5.63 \cdot 10^{-4}$
$5.00 \cdot 10^8$	$5 \cdot 10^{-4}$	$6.25 \cdot 10^{-2}$	32.77	$-8.70 \cdot 10^{-3}$	$6.14 \cdot 10^{-4}$
$8.00 \cdot 10^8$	$5 \cdot 10^{-4}$	$1.00 \cdot 10^{-1}$	40.81	$-1.12 \cdot 10^{-2}$	$6.90 \cdot 10^{-4}$
$1.75 \cdot 10^9$	$5 \cdot 10^{-4}$	$2.19 \cdot 10^{-1}$	47.36	$-2.11 \cdot 10^{-2}$	$9.32 \cdot 10^{-4}$
$2.00 \cdot 10^9$	$5 \cdot 10^{-4}$	$2.50 \cdot 10^{-1}$	47.14	$-2.43 \cdot 10^{-2}$	$9.96 \cdot 10^{-4}$

table 7.3 easily proves that we do not exceed the transition values ε_1 and ε_2 with our excitation amplitude $A_0 = 2.63 \cdot 10^{-6}$. Furthermore, the third column of the table displays resulting variation of the crack density c, which is changed in a range from $c = 0.005$ to $c = 0.25$ due to the variation of our parameter N_0. This range of crack density approximately represents the boundaries of the underlying combined model, which was derived on the fundamental assumption that the crack density is low, such that crack interactions can be neglected and the strain fields of each crack do not interfere. The lower limitation is given due to signal processing and the resulting FFT resolution in this research, where second harmonic strain amplitudes A_2 of a magnitude smaller than $A_2 < 10^{-10}$ cannot be detected. Therefore, this approach is limited to β_{RSC} values above $\beta_{RSC} > 3$ corresponding to crack density c above $c > 0.005$ with the given parameters. Figure 7.4 shows the qualitative course of the strain amplitude ratio $\frac{A_2}{A_1^2}$ over the number of cracks per cubic meter N_0. In addition, the graph 7.3 (a) is depicted in a discretized manner using the same x-axis values as for the simulations in the same figure. Note that both graphs have different y-axes,

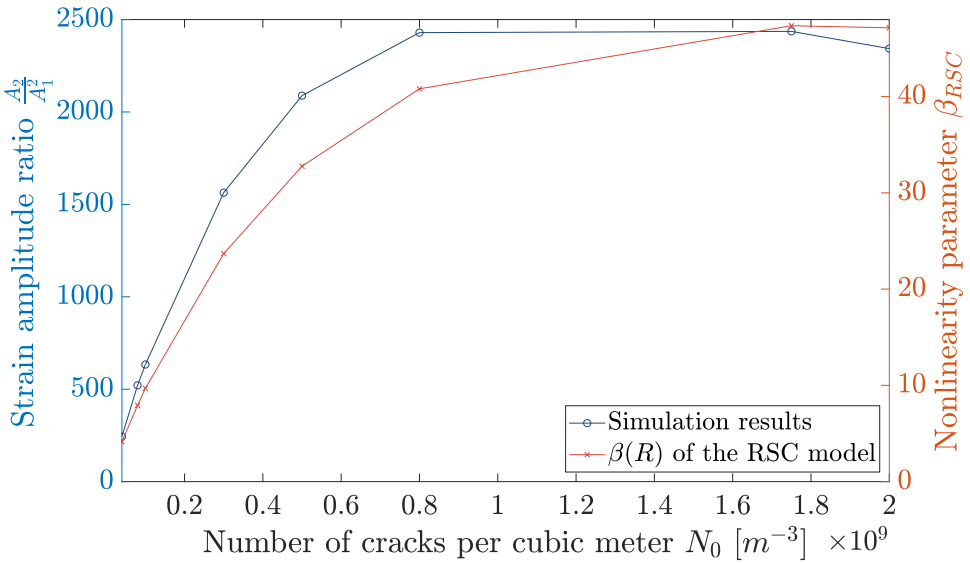

Figure 7.4: Dependency of the simulated strain amplitude ratio $\frac{A_2}{A_1^2}$ (red line with circled data points) assigned to the left y-axis and dependency of the acoustic nonlinearity parameter β_{RSC} (blue line with crossed date points) assigned to the right y-axis on the number of cracks per cubic meter N_0

such that this display does not allow a quantitative statement. The only, but still very important statement we can conclude from this plot, is that the utilized numerical algorithm and the resulting strain amplitude ratio $\frac{A_2}{A_1^2}$ represent the dependency of the combined model on the crack parameter N_0 quantitatively in a very good approach. The fact, that the strain amplitude ratio starts decreasing earlier than the actual acoustic nonlinearity parameter according to equation 7.3, suggests that the limiting assumption of the underlying modeling approach that the crack density has to be low, is reached somewhere around $c \approx 0.2$.

7.2.2 Crack Radius R

For the variation of the crack radius R the same condition as for the variation of the number of cracks per cubic meter N_0 apply. This time N_0 is set to the default value of $N_0 = 3 \cdot 10^8 m^{-3}$ from Hoffmann et al., while R is varied. As seen in figure 7.3 and equation 7.3, the acoustic nonlinearity parameter β_{RSC} is much more sensitive

to changes of the crack radius R. Therefore, R has to be varied only in a small range from $R = 0.0003$m to $R = 0.001$m to reach the discussed limits of the model and the signal processing. A complete schedule of the simulation parameters can be found in table 7.4. Repeatedly, it shows that we stay within the transitions ε_1 and ε_2 for all simulations. In this section the ratio of strain amplitudes $\frac{A_2}{A_1^2}$ as well as

Table 7.4: Parameter variation of R and the resulting values for the crack density c, β_{RSC} and transitions ε_1,ε_2

$\boldsymbol{R}$	$\boldsymbol{N_0}$	$\boldsymbol{c}$	$\boldsymbol{\beta_{RSC}}$	$\boldsymbol{\varepsilon_1}$	$\boldsymbol{\varepsilon_2}$
$3.00 \cdot 10^{-4}$	$3 \cdot 10^8$	$8.10 \cdot 10^{-3}$	3.92	$-9.50 \cdot 10^{-3}$	$8.39 \cdot 10^{-4}$
$4.00 \cdot 10^{-4}$	$3 \cdot 10^8$	$1.92 \cdot 10^{-2}$	11.25	$-7.80 \cdot 10^{-3}$	$6.58 \cdot 10^{-4}$
$5.00 \cdot 10^{-4}$	$3 \cdot 10^8$	$3.75 \cdot 10^{-2}$	23.69	$-7.20 \cdot 10^{-3}$	$5.63 \cdot 10^{-4}$
$6.00 \cdot 10^{-4}$	$3 \cdot 10^8$	$6.48 \cdot 10^{-2}$	40.11	$-7.40 \cdot 10^{-3}$	$5.16 \cdot 10^{-4}$
$7.00 \cdot 10^{-4}$	$3 \cdot 10^8$	$1.03 \cdot 10^{-1}$	57.73	$-8.20 \cdot 10^{-3}$	$4.97 \cdot 10^{-4}$
$9.00 \cdot 10^{-4}$	$3 \cdot 10^8$	$2.19 \cdot 10^{-1}$	85.24	$-1.17 \cdot 10^{-2}$	$5.18 \cdot 10^{-4}$
$1.00 \cdot 10^{-3}$	$3 \cdot 10^8$	$3.00 \cdot 10^{-1}$	92.37	$-1.49 \cdot 10^{-2}$	$5.49 \cdot 10^{-4}$

the acoustic nonlinearity parameter β_{RSC} is plotted for a varying crack radius R. As for the number of crack per cubic meter, the utilized numerical algorithm and the resulting strain amplitude ratio $\frac{A_2}{A_1^2}$ also represent the dependency of the combined model on the crack radius R very well in a quantitative way. Similarly, getting close to a critically high crack density c, which marks the limit of the underlying modeling approach by increasing R, results in an early decrease of the strain amplitude ratio.

In conclusion, the numerical algorithm with the strain amplitude ratio $\frac{A_2}{A_1^2}$ follows the expected dependency on the crack parameter N_0 and R. This confirms that the quadratic part of combined model from Hoffmann et al. in combination with the Kurganov-Levy algorithm conserve the material's behavior for changing crack parameters. The observation of early decreasing strain amplitude ratios for comparatively high crack densities supported the hypothesis that the not explicitly quantified limi-

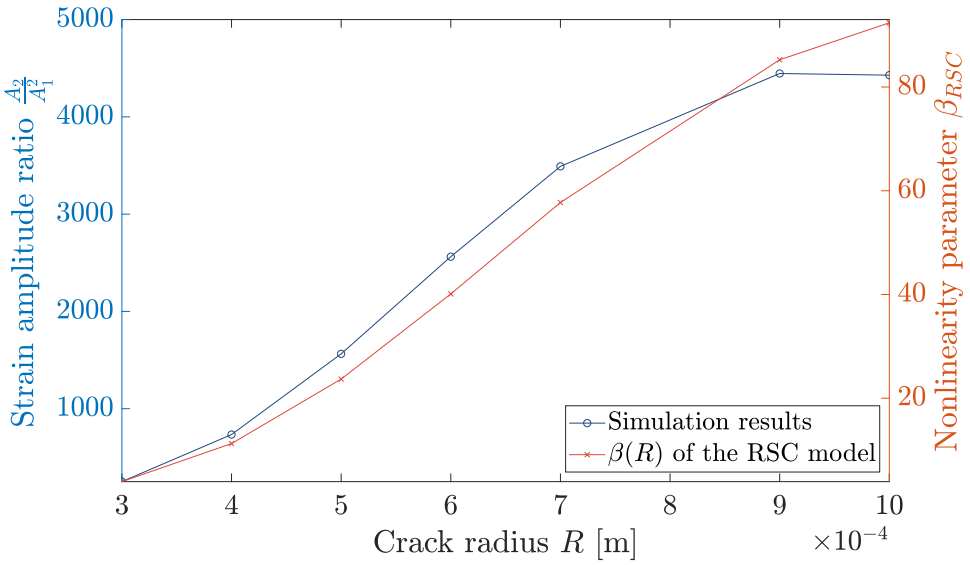

Figure 7.5: Dependency of the simulated strain amplitude ratio $\frac{A_2}{A_1^2}$ (red line with circled data points) assigned to the left y-axis and dependency of the acoustic nonlinearity parameter β_{RSC} (blue line with crossed data points) assigned to the right y-axis on the crack radius R

tation of a "low" crack density for validity of the combined model lies slightly above $c = 0.2$. In contrast, relating to [46], crack interactions become relevant around crack densities of $c \approx 0.35$. In this case, the observed phenomenon has to result from numerical or analysis inaccurateness. At this point, the origin of this behavior cannot be clearly identified.

7.3 Full Model - Dependency on Crack Parameters

This section investigates the full combined model from Hoffmann et al. by applying high excitation amplitudes of $A_0 = 2 \cdot 10^{-4}$. This strain excitation relates to a displacement excitation of approximately 38 nm. Such high displacement are usually not the case in the field of nondestructive evaluation. Nevertheless, the investigation of these high excitations help to better understand the evolution of nonlinear effects and the underlying physical processes in the material in general. Furthermore, such studies are of high interest for rating the materials' state and possible fatigue in

misuse scenarios.

Besides theoretical considerations, there does not exist much literature on experimental or numerical data for high-amplitude, ultrasonic excitation. According to Solodov and Korshak [47], materials with strong nonlinearity, e.g. due to microcracks, tend to exhibit subharmonic bifurcations, dynamic instability, and chaos. Such microcracks can be considered to represent a strongly nonlinear oscillator leading to some kind of nonlinear storage ("memory") effect. As one of the rare publications they utilize experimental data with high strain excitations for investigation of these effects.

Since it is unclear what to expect for the numerical simulations with such high excitation amplitudes and strong nonlinearity and for the dependency on the crack parameters, we start with a familiar display. It is important to note that all the following displayed results only hold for the chosen strain excitation amplitude of $A_0 = 2 \cdot 10^{-4}$ and general conclusions have to be treated very cautious. Figure 7.6 shows the ratio $\frac{A_2}{A_1^2}$ of the first and second harmonic amplitude obtained from the numerical results plotted over the acoustic nonlinearity parameter β_{RSC} similar to section 7.1. Display 7.6 (a) shows the course of the amplitude ratio over a wide range of corresponding acoustic nonlinearity parameter up to extremely high values of $\beta_{RSC} = 1000$. While we can see in 7.6 (b), that the linear relationship from section 7.1 between amplitude ratio $\frac{A_2}{A_1^2}$ and acoustic nonlinearity parameter β_{RSC} holds up to $\beta_{RSC} \approx 25$, this relationship clearly changes for higher β_{RSC} values in combination the considered high excitation amplitudes. Even though we did not cross the transition values ε_1 and ε_2 with the high excitation amplitude up to $\beta_{RSC} \approx 250$ (as mentioned earlier, the transitions change for different β_{RSC}), this linear relationship, which is theoretically considered to hold until we crossed one of the transitions breaks down. This observation is supported by looking at the wave form after propagation.

As we can see in figure 7.7, with increasing nonlinearity the initially smooth wave

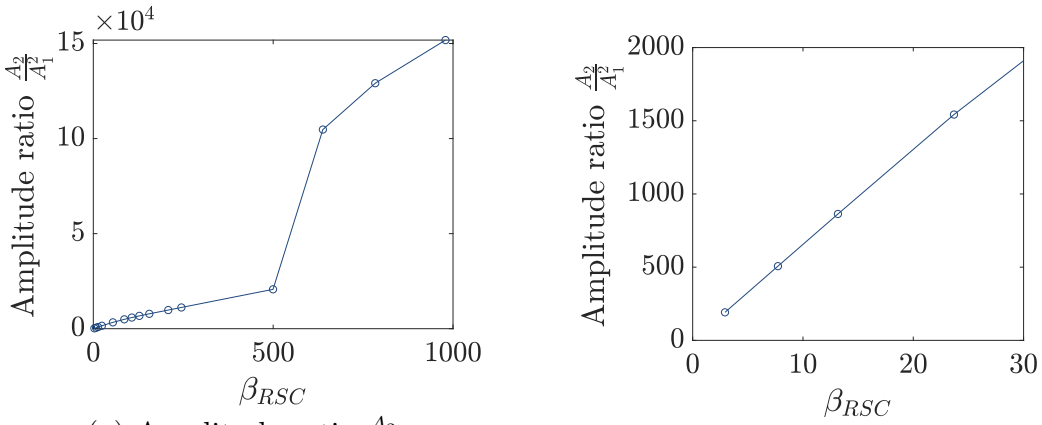

(a) Amplitude ratio $\frac{A_2}{A_1^2}$ up to $\beta_{RSC} = 1000$

(b) Zoomed in view at low β_{RSC}

Figure 7.6: Strain amplitude ratio $\frac{A_2}{A_1^2}$ with corresponding acoustic nonlinearity parameter β_{RSC}

form starts to change into a sawtooth shaped form with steep, discontinuous-like slopes relating to shock wave development. The development of such a sawtooth profile is well known and is what can be expected for quadratic (classic) nonlinearity - as incorporated in this model - according to Van Den Abeele et al. [48]. This slowly but steady shock wave development phenomenon suspects the breakdown of the linear relationship between $\frac{A_2}{A_1^2}$ and β_{RSC}, even before real shock waves occur. This is might be due to the slowly steepening of the propagation direction turned away flank and slowly flattening of the front flank, where the energy transported in the wave is not linearly distributed between A_1^2 and A_2. The strong decrease of amplitude in figures 7.7 (e) and (f) is probably caused by the sudden release of energy during shock formation, where all the higher harmonic get strongly excited and other physical effect become significantly important. At this point it should be mentioned, that the study of shock wave phenomena goes beyond the scope of this research and is not investigated any further. Nevertheless, since this shock wave formation and resulting breakdown of the considered relationship obviously did not occur for low excitation amplitudes (see 7.2), this phenomenon seems to be excitation-dependent.

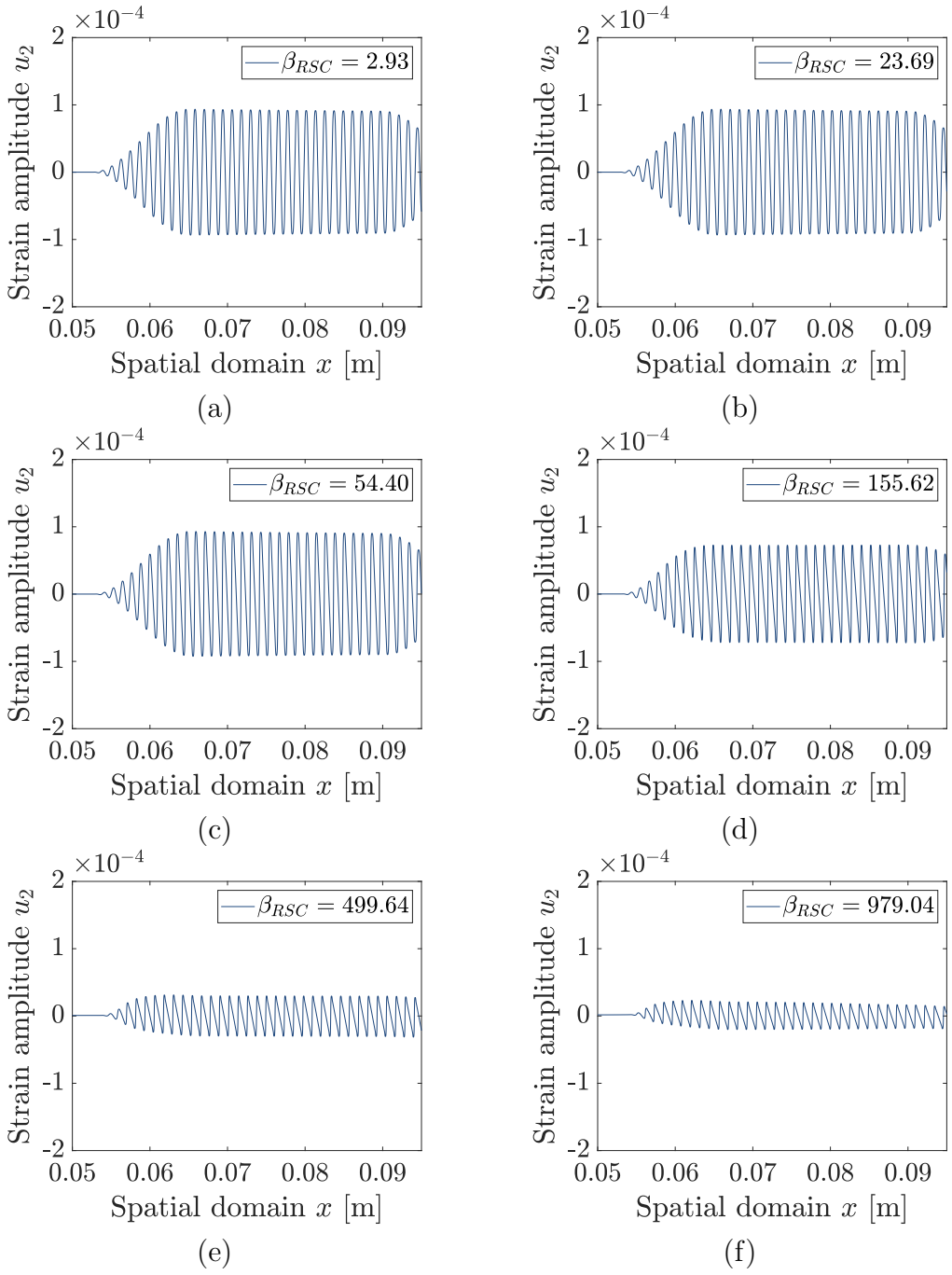

Figure 7.7: Numerical results for a high-amplitude strain wave after propagation for different β_{RSC} values. For low β_{RSC} (a) the wave form looks undistorted. From (b) to (c) the linear relationship breaks down. (d) already depicts the characteristic sawtooth waveform. And (e) and (f) clearly indicate shock wave formation

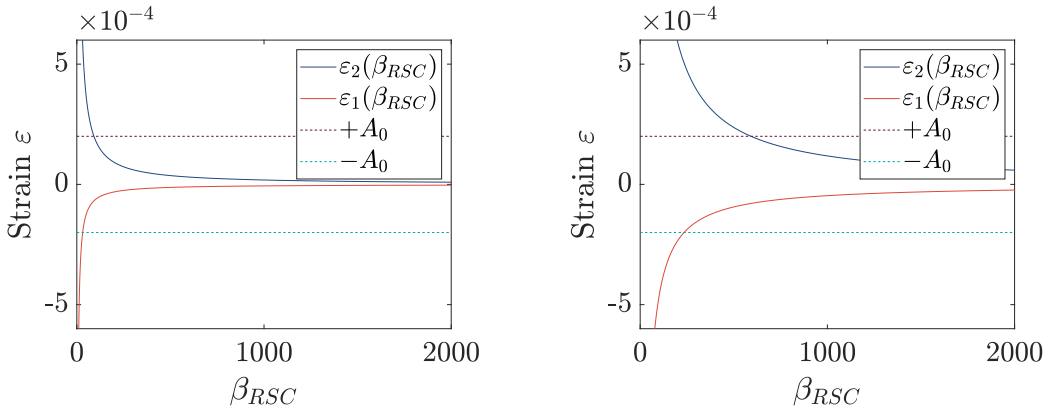

(a) $N_0 = 4 \cdot 10^7\ [m^{-3}]$ (b) $N_0 = 3 \cdot 10^8\ [m^{-3}]$

Figure 7.8: Example of the dependency of the transitions ε_1 and ε_2 on the acoustic nonlinearity parameter β_{RSC} for different numbers of cracks (a) $N_0 = 4 \cdot 10^7\ [m^{-3}]$ and (b) $N_0 = 3 \cdot 10^8 [m^{-3}]$

Even after the breakdown of this linear dependency around $\beta_{RSC} \approx 25$ for a high excitation amplitude, the second harmonic generation in general does not seem to be chaotic or randomly distributed for a very strong nonlinearity as it might be suspected according to Solodov and Korshak [47]. However, more data points in general and some exceeding $\beta_{RSC} = 1000$ are necessary to make more detailed statements about this relationship. But already the observation, that the second harmonic generation appears not to be chaotic, enables us to take a deeper look into what happens around the transitions ε_1 and ε_2 as well as for different crack parameters.

Note that in figure 7.6 (a), we did not exceed one of the transitions values up to $\beta_{RSC} \approx 240$ and not both transitions at same up to $\beta_{RSC} \approx 480$. Therefore, only the four most right data points in this graphic show the results for completely crossed transitions and the fifth data point for only one exceeded transition, while all the other data points only represent the quadratic part of the combined model. With this information, figure 7.6 suggests that it makes a big difference if you only cross the transitions slightly (4th data points from the right) or if you go further above these values (three furthest right data points).

For a better illustration how it is possible to cross the transitions completely, partially, slightly or clearly, all with the same constant excitation amplitude and different β_{RSC1} and β_{RSC2}, figure 7.8 shows the shift of the transitions for two parameter sets. The curved solid lines show the course of the lower transition ε_1 and upper transition ε_2, respectively over acoustic nonlinearity parameter β_{RSC}. The dashed lines represent the maximum positive and negative values of our strain excitation amplitude. The intersection of these dashed lines with the solid lines denote the corresponding β_{RSC} at which we cross a specific transition. Furthermore, figure 7.8 depicts that the upper and lower transitions are not located symmetrically around the zero strain, which is due to the definition of the Young's moduli in the Bilinear Stiffness model. The important takeaway from this display is that we need to recalculate the transitions whenever we change a single crack parameter additionally to the one parameter, e.g. N_0 and R we want to investigate.

The overall goal of this thesis is to study the dependency of the first and second harmonic amplitude on the macroscopic crack parameters N_0 (number of cracks per cubic meter) and R (crack radius). Section 7.2 already studied this dependency for the quadratic part of the model. Beyond that, we want to see how this dependency changes around and above the transitions where the complete combined model comes into consideration. In the subsequent part, this change of dependency is examined.

7.3.1 Number of Cracks per cubic meter N_0

Figure 7.9 presents the dependency of the strain amplitude ratio $\frac{A_2}{A_1^2}$ determined from the numerical results for three different numbers of cracks per cubic meter N_0 slightly below the transitions ε_1 and ε_2, with just one transition crossed, slightly above both transitions and clearly above both transitions. The values for N_0 are displayed in table 7.5 and the crack radius was kept constant at $R = 5 \cdot 10^{-4}$m. Fist and foremost, note that the obtained results only provide a brief qualitative idea on how

Table 7.5: Variation of the parameter N_0

$\boldsymbol{N_{01}}[m^{-3}]$	$\boldsymbol{N_{02}}\ [m^{-3}]$	$\boldsymbol{N_{03}}\ [m^{-3}]$
$4 \cdot 10^7$	$3 \cdot 10^8$	$8 \cdot 10^8$

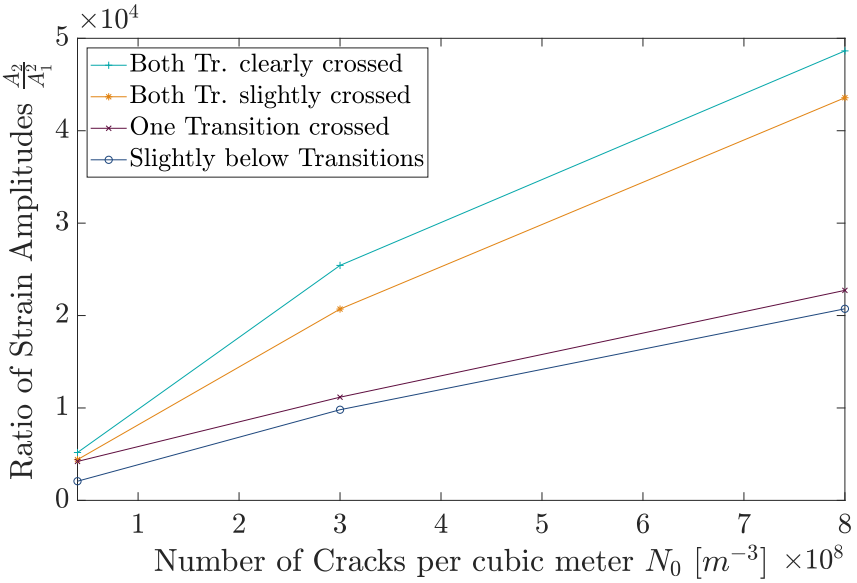

Figure 7.9: Dependency of the simulated strain amplitude ratio $\frac{A_2}{A_1^2}$ on the number of cracks per cubic meter N_0 for below, partially, completely, and far above the transitions, where the full model comes into consideration

the amplitude ratio behaves for different numbers of cracks per cubic meters around and above the transitions, since the data representing these trends is very sparse.

Furthermore, the classification "slightly below transitions", "one transition crossed", "both transitions slightly crossed", and "both transitions clearly crossed" is chosen to be very indistinct on purpose. Because, it only states that the particular condition is fulfilled somehow, but it does not draw the whole picture. This means for example, that there exist data points for "both transitions slightly crossed", where the upper transition is indeed only crossed by $\approx 10^{-6}$, but due to the asymmetry of the transitions, the lower transition might be already crossed by $\approx 10^{-5}$. Contrary, there are examples where both transitions are in fact only exceed very slightly because the

course of transitions allowed this setup.

For the sake of completeness another important notice should be considered. The grading of exceeding the transitions is based on the values ε_1 and ε_2 together with our initial strain amplitude $A_0 = 2{\cdot}10^{-4}$. However, in the previous chapter we showed that the initial wave divides into two equivalent waves traveling into different directions with only half the original amplitudes for $t > 0$. As a consequence, after both waves are completely separated they do not exceed the transition values anymore in any presented example in this thesis. The latter note can be neglected for the presented results, since waves are only fully separated for 1/6 of the total propagation distance.

Despite all mentioned restrictions of comparability, the obtained results still provide us a first approach to understand the combined model from Hoffmann et al. and some information about the dependency of the amplitudes ratio on the crack parameters. If we compare Figure 7.9 with the corresponding quadratic investigation 7.4, it can be seen that the general trend of receiving increased amplitude ratios for an increasing volume fraction of cracks remains the same over all stages of the model. Moreover, figure 7.9 suggests that the amplitude ratio (representing the overall nonlinearity) shows the highest value for crossing both transitions clearly, the second highest for crossing both transitions slightly, and so on over all considered N_0. This matches the physical intuition that crossing one or both transitions increases the nonlinearity of the systems. An interesting trend that we can deduct from figure 7.9 is that, the amplitude ratio changes stronger for an increasing number of cracks per volume as soon as both transitions are exceeded, while below the transitions or with just one transition crossed it does not change that much. This suggests that an increasing number of cracks per volume influence the overall nonlinearity of the combined system much stronger, than the nonlinearity of the quadratic part. As a consequence, it seems like the physical complete closing and complete opening of the cracks become the dominant source of nonlinearity above a certain number of cracks

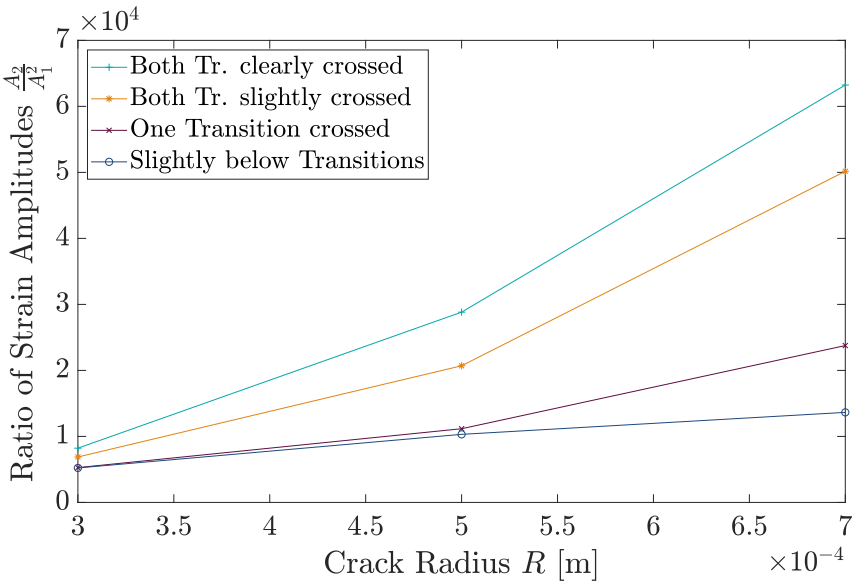

Figure 7.10: Dependency of the simulated strain amplitude ratio $\frac{A_2}{A_1^2}$ on the crack radius R for below, partially, completely, and far above the transitions, where the full model comes into consideration

per volume.

7.3.2 Crack Radius R

According to the variation of N_0, figure 7.10 shows the dependency of the strain amplitude ratio $\frac{A_2}{A_1^2}$ determined from the numerical results for three different values of the crack radius R. Again, this dependency is depicted slightly below the transitions ε_1 and ε_2, with just one transition crossed, slightly above both transitions and clearly above both transitions. The values for R are displayed in table 7.6 and the number of cracks per cubic meter remained constant at $N_0 = 3 \cdot 10^8$ $[m^{-3}]$.

Table 7.6: Variation of the parameter R

$\boldsymbol{R_{01}}$ [m]	$\boldsymbol{R_{02}}$ [m]	$\boldsymbol{R_{03}}$ [m]
$3 \cdot 10^{-4}$	$5 \cdot 10^{-4}$	$7 \cdot 10^{-4}$

As for discussion above, the restrictions of comparability apply to this crack parameter as well as for N_0. But again, figure 7.10 shows some interesting general trends. Similarly to N_0, a comparison of figure 7.10 with the examination of the quadratic part 7.5 both graphs show the same intuitive trend that the amplitude ratio increases for bigger crack radii. Besides that, figure 7.10 discloses the same trends for the amplitude ratio over a varied crack radius R as we saw it for the number of cracks per volume N_0. The ratio of amplitudes exposes its highest values and therefore the highest nonlinearity if we cross both transitions clearly and respective second and third highest values are reached for crossing both transitions slightly and crossing only one transition. Also, the nonlinearity of the whole combined model is more sensitive to an increased crack radius compared to the nonlinearity of the quadratic part or a state where we only cross one transition.

Comparing the influence of the number of cracks per volume to the influence of the crack radius on the overall nonlinearity represented by $\frac{A_2}{A_1^2}$ concludes that both crack parameters introduce the effects for increasing values. This is what we expect, since they can be summarized by the crack density $c = N_0 R^3$ and an increase of either parameter results in and a higher crack density and a stronger nonlinearity of the system. The observation that the crack radius R influences the nonlinearity of the system stronger than the number of cracks per volume fraction as shown in 7.3 cannot be confirmed with these results, since a comparison based on absolute values of the strain ratios between the two plots 7.9 and 7.10 is not valid due to the mentioned comparability restrictions.

CHAPTER 8
CONCLUSION AND FUTURE WORK

8.1 Conclusion

This research investigated the excitation-dependent behavior of distributed microcracks based on the combined model from Hoffmann et al. [18] by utilizing a numerical, semi-discrete Kurganov-Levy algorithm.

The first step of this research was the reformulation of the governing problem into a hyperbolic system of conservation laws for the implementation in the numerical algorithm. The validation of the implementation and appropriate choice of computational parameters was successfully depicted by the investigation of a linear problem. The extension to the quadratic nonlinearity part of the combined model with low excitation amplitudes proved that the numerical approach leads to accurate results over a broad range of different acoustic nonlinearity parameters β_{RSC}. The high nonlinearities considered in this work caused an exceedance of the point where the first harmonic amplitude is not much higher than the second harmonic amplitude anymore, and therefore approximations like the pertubation method do not hold beyond this point. However, the numerical algorithm still provided accurate results.

Furthermore, it was shown that a variation of the crack parameters N_0, number of cracks per cubic meter, and R, crack radius, described the expected behavior of the strain amplitude ratio $\frac{A_2}{A_1^2}$ for the quadratic nonlinearity part of the model adequately. Only for high crack densities close to a limiting crack density (not quantified) of the combined model the trends diverged observably. The numerical results in this section have been compared to the trends of the acoustic nonlinearity parameter.

Finally, the excitation with high amplitudes was investigated. These results show

strong nonlinear effects, such as shock formation for corresponding high β_{RSC} values. The amplitude ratios obtained constantly increased for stronger nonlinearity and showed a sudden increase shortly after crossing both transitions, which incorporates the whole combined model. A following crack parameter variation around the transitions presented meaningful trends of the strain amplitude ratio. This section lead to the interesting observation that the amplitude ratio, and therefore, the overall nonlinearity of the system increases stronger for different crack parameters if both transitions are completely crossed. Consequently, it seems like the physical complete closing and complete opening of the cracks becomes the dominant source of nonlinearity above a certain number of cracks per volume or above a certain crack radius, respectively.

The analysis of the results suggested that the numerically determined solutions presented can only be interpreted qualitatively, since they repeatedly displayed corresponding trends to the expected solutions. However, quantitative statements could not be derived from the results. This is possibly due to: strong nonlinear effects including shock formation, such that significant excitation of higher harmonics and not just the second harmonic takes place; numerical dissipation, which might not be neglectable above a certain point where steeper gradients exceed the limits of the spatial discretization; and signal-processing reasons, that limited the resolution and amplitude accuracy of the FFT analysis. Despite these restrictions when it comes to the quantitative interpretation of the result, the qualitative trends matched the known/expected behavior and physical intuition without exception. Therefore, the general appropriateness of the modified numerical algorithm for the study of the excitation-dependent nonlinear behavior of distributed microcracks was presented and first trends of this behavior could be demonstrated for different crack parameters. Moreover, the numerical results prove that the level of nonlinearity of cracked materials has a strong dependency on the amplitude of excitation.

8.2 Future Work

This study showed that the consulted numerical algorithms provides a powerful tool for the investigation of crack materials exhibiting strong nonlinear effects. It only provides a small insight into the dependency of the nonlinearity on crack parameters. In future work, the dependency has to be further examined. A more representative investigation based on bigger set of data points compared to the results in section 7.3 is crucial for deducting more meaningful statements on this dependency. Likewise, a more detailed investigation of the influence of the transitions, where the quadratic nonlinearity part of the model evolves into the complete combined model should be subject of future studies.

Some numerical results demonstrated that the utilized numerical solver together with the chosen spatial discretization comes close to its limits for high amplitudes combined with high nonlinearity. Especially, if one wants to derive quantitative statements about this model, moving on to another numerical algorithm might be inevitable. Otherwise, the computational time of the Kurganov-Levy scheme will exceed reasonable limits. Therefore, highly developed software packages, e.g. ClawPack that support parallel computing as well as mesh refinement in discontinuous regions might overcome these challenges. The main disadvantage of ClawPack particularly, is the necessity of (approximate) Riemann solvers for providing a solution to the governing problem. Nevertheless, in future work this switch might be considered.

Finally, an experimental setup that allows the excitation of cracked specimens with high amplitudes would be important to compare, approve, or disapprove phenomena observed in the simulations.

REFERENCES

[1] K. Matlack, J.-Y. Kim, L. Jacobs, and J. Qu, "Review of second harmonic generation measurement techniques for material state determination in metals," *Journal of Nondestructive Evaluation*, vol. 34, no. 1, p. 273, 2015.

[2] T. Mura, *Micromechanics of defects in solids*. Springer Science & Business Media, 2013.

[3] D. Broda, W. Staszewski, A Martowicz, T Uhl, and V. Silberschmidt, "Modelling of nonlinear crack–wave interactions for damage detection based on ultrasound—a review," *Journal of Sound and Vibration*, vol. 333, no. 4, pp. 1097–1118, 2014.

[4] B. Budiansky and R. J. O'connell, "Elastic moduli of a cracked solid," *International journal of Solids and structures*, vol. 12, no. 2, pp. 81–97, 1976.

[5] H Horii and S Nemat-Nasser, "Overall moduli of solids with microcracks: Load-induced anisotropy," *Journal of the Mechanics and Physics of Solids*, vol. 31, no. 2, pp. 155–171, 1983.

[6] M. L. Kachanov, "A microcrack model of rock inelasticity part i: Frictional sliding on microcracks," *Mechanics of Materials*, vol. 1, no. 1, pp. 19–27, 1982.

[7] M. Kachanov, "Effective elastic properties of cracked solids: Critical review of some basic concepts," *Applied Mechanics Reviews*, vol. 45, no. 8, pp. 304–335, 1992.

[8] Y. Zhao, Y. Qiu, L. J. Jacobs, and J. Qu, "Frequency-dependent tensile and compressive effective moduli of elastic solids with randomly distributed two-dimensional microcracks," *Journal of Applied Mechanics*, vol. 82, no. 8, p. 081 006, 2015.

[9] O. Buck, W. Morris, and J. M. Richardson, "Acoustic harmonic generation at unbonded interfaces and fatigue cracks," *Applied Physics Letters*, vol. 33, no. 5, pp. 371–373, 1978.

[10] J. M. Richardson, "Harmonic generation at an unbonded interface—i. planar interface between semi-infinite elastic media," *International Journal of Engineering Science*, vol. 17, no. 1, pp. 73–85, 1979.

[11] I. Y. Solodov, "Ultrasonics of non-linear contacts: Propagation, reflection and nde-applications," *Ultrasonics*, vol. 36, no. 1-5, pp. 383–390, 1998.

[12] V. E. Nazarov and A. M. Sutin, "Nonlinear elastic constants of solids with cracks," *The Journal of the Acoustical Society of America*, vol. 102, no. 6, pp. 3349–3354, 1997.

[13] J. H. Cantrell, "Quantitative assessment of fatigue damage accumulation in wavy slip metals from acoustic harmonic generation," *Philosophical Magazine*, vol. 86, no. 11, pp. 1539–1554, 2006.

[14] J. H. Cantrell, "Acoustic nonlinearity from cracks," in *Ultrasonic nondestructive evaluation: Engineering and biological material characterization*. CRC press, 2003, ch. 6.3.8, pp. 424–429.

[15] T. Oberhardt, J.-Y. Kim, J. Qu, and L. J. Jacobs, "A contact mechanics based model for partially-closed randomly distributed surface microcracks and their effect on acoustic nonlinearity in rayleigh surface waves," in *AIP Conference Proceedings*, AIP Publishing, vol. 1706, 2016, pp. 20–24.

[16] M. Rjelka, B. Köhler, and A. Mayer, "Nonlinear effects of micro-cracks on long-wavelength symmetric lamb waves," *Ultrasonics*, vol. 90, pp. 98–108, 2018.

[17] R. A. Guyer and P. A. Johnson, "Nonlinear mesoscopic elasticity: Evidence for a new class of materials," *Physics today*, vol. 52, pp. 30–36, 1999.

[18] K. Hoffmann, J.-Y. Kim, K. Scott, J. Qu, and L. J. Jacobs, "Excitation-dependent nonlinear behavior of distributed microcracks," in *AIP Conference Proceedings*, AIP Publishing, vol. 2102, 2019, pp. 20–39.

[19] G. Odette, M. Alinger, and B. Wirth, "Recent developments in irradiation-resistant steels," *Annu. Rev. Mater. Res.*, vol. 38, pp. 471–503, 2008.

[20] G. R. Odette, "Recent progress in developing and qualifying nanostructured ferritic alloys for advanced fission and fusion applications," *Jom*, vol. 66, no. 12, pp. 2427–2441, 2014.

[21] J. H. Kim, T. S. Byun, D. T. Hoelzer, S.-W. Kim, and B. H. Lee, "Temperature dependence of strengthening mechanisms in the nanostructured ferritic alloy 14ywt: Part i — mechanical and microstructural observations," *Materials Science and Engineering: A*, vol. 559, pp. 101–110, 2013.

[22] K. F. Graff, *Wave motion in elastic solids*. Courier Corporation, 2012.

[23] J. Achenbach, *Wave propagation in elastic solids*. Elsevier, 2012, vol. 16.

[24] K. D. Hoffmann, "Excitation-dependent nonlinear behavior of distributed microcracks," M.S. Thesis, Georgia Institute of Technology, Atlanta, 2018.

[25] L. Debnath, *Nonlinear partial differential equations for scientists and engineers*. Springer Science & Business Media, 2011.

[26] R. J. LeVeque and R. J. Leveque, *Numerical methods for conservation laws*. Springer, 1992, vol. 132.

[27] G. B. Whitham, *Linear and nonlinear waves*. John Wiley & Sons, 2011, vol. 42.

[28] M. E. Taylor, *Partial differential equations. 3, Nonlinear equations*. Springer, 1991.

[29] E. Godlewski and P.-A. Raviart, *Numerical approximation of hyperbolic systems of conservation laws*. Springer Science & Business Media, 2013, vol. 118.

[30] J. W. Thomas, *Numerical partial differential equations: conservation laws and elliptic equations*. Springer Science & Business Media, 2013, vol. 33.

[31] R. J. LeVeque *et al.*, *Finite volume methods for hyperbolic problems*. Cambridge university press, 2002, vol. 31.

[32] E. Tadmor, "Approximate solutions of nonlinear conservation laws," in *Advanced numerical approximation of nonlinear hyperbolic equations*, Springer, 1998, pp. 1–149.

[33] D. L. Powers, *Boundary value problems: and partial differential equations*. Academic Press, 2009.

[34] J. W. Thomas, *Numerical partial differential equations: finite difference methods*. Springer Science & Business Media, 2013, vol. 22.

[35] A. Kurganov and D. Levy, "A third-order semidiscrete central scheme for conservation laws and convection-diffusion equations," *SIAM Journal on Scientific Computing*, vol. 22, no. 4, pp. 1461–1488, 2000.

[36] A. Kurganov and E. Tadmor, "New high-resolution central schemes for nonlinear conservation laws and convection–diffusion equations," *Journal of Computational Physics*, vol. 160, no. 1, pp. 241–282, 2000.

[37] H. Nessyahu and E. Tadmor, "Non-oscillatory central differencing for hyperbolic conservation laws," *Journal of computational physics*, vol. 87, no. 2, pp. 408–463, 1990.

[38] E. Tadmor, "A review of numerical methods for nonlinear partial differential equations," *Bulletin of the American Mathematical Society*, vol. 49, no. 4, pp. 507–554, 2012.

[39] J. Peiró and S. Sherwin, "Finite difference, finite element and finite volume methods for partial differential equations," in *Handbook of materials modeling*, Springer, 2005, pp. 2415–2446.

[40] D. Levy, G. Puppo, and G. Russo, "Compact central weno schemes for multidimensional conservation laws," *SIAM Journal on Scientific Computing*, vol. 22, no. 2, pp. 656–672, 2000.

[41] J. Balbás and E. Tadmor, "Centpack version 1.0 - user's guide," *online at https://www.cscamm.umd.edu/centpack/documentation/CP_user_guide.pdf*, 2006.

[42] S. Gottlieb, C.-W. Shu, and E. Tadmor, "Strong stability-preserving high-order time discretization methods," *SIAM review*, vol. 43, no. 1, pp. 89–112, 2001.

[43] T. Meurer, "Wave propagation in hysteretic media," M.S. Thesis, Georgia Institute of Technology, Atlanta, 2000.

[44] S. Küchler, T. Meurer, L. J. Jacobs, and J. Qu, "Two-dimensional wave propagation in an elastic half-space with quadratic nonlinearity: A numerical study," *The Journal of the Acoustical Society of America*, vol. 125, no. 3, pp. 1293–1301, 2009.

[45] J.-Y. Kim, A Baltazar, and S. Rokhlin, "Ultrasonic assessment of rough surface contact between solids from elastoplastic loading–unloading hysteresis cycle," *Journal of the Mechanics and Physics of Solids*, vol. 52, no. 8, pp. 1911–1934, 2004.

[46] M. Kachanov, "Effective elastic properties of cracked solids," Tech. Rep., 1993.

[47] I. Y. Solodov and B. A. Korshak, "Instability, chaos, and "memory" in acoustic-wave–crack interaction," *Physical review letters*, vol. 88, no. 1, p. 014 303, 2001.

[48] K.-A. Van Den Abeele, P. A. Johnson, and A. Sutin, "Nonlinear elastic wave spectroscopy (news) techniques to discern material damage, part i: Nonlinear wave modulation spectroscopy (nwms)," *Journal of Research in Nondestructive Evaluation*, vol. 12, no. 1, pp. 17–30, 2000.